HHS Public Access

Author manuscript

Mol Cell. Author manuscript; available in PMC 2019 March 01.

Published in final edited form as:

Mol Cell. 2018 March 01; 69(5): 729–743.e7. doi:10.1016/j.molcel.2018.02.005.

Dynamic Regulation of Long-Chain Fatty Acid Oxidation by a Noncanonical Interaction between the MCL-1 BH3 Helix and VLCAD

Silvia Escudero[1], **Elma Zaganjor**[2], **Susan Lee**[1], **Christopher P. Mill**[3], **Ann M. Morgan**[1], **Emily B. Crawford**[1], **Jiahao Chen**[4], **Thomas E. Wales**[5], **Rida Mourtada**[1], **James Luccarelli**[1], **Gregory H. Bird**[1], **Ulrich Steidl**[4], **John R. Engen**[5], **Marcia C. Haigis**[2], **Joseph T. Opferman**[3,*], and **Loren D. Walensky**[1,6,*]

[1]Department of Pediatric Oncology and the Linde Program in Cancer Chemical Biology, Dana-Farber Cancer Institute, Boston, MA 02215, USA

[2]Department of Cell Biology, Harvard Medical School, Boston, MA 02115, USA

[3]Department of Cell and Molecular Biology, St. Jude Children's Research Hospital, Memphis, TN 38105, USA

[4]Department of Medicine, Albert Einstein College of Medicine; Department of Cell Biology, Albert Einstein College of Medicine, Bronx, NY 10461, USA

[5]Department of Chemistry and Chemical Biology, Northeastern University, Boston, MA 02115, USA

SUMMARY

MCL-1 is a BCL-2 family protein implicated in the development and chemoresistance of human cancer. Unlike its anti-apoptotic homologs, *Mcl-1* deletion has profound physiologic consequences, indicative of a broader role in homeostasis. We report that the BCL-2 homology 3

[*]Correspondence: Loren D. Walensky, M.D., Ph.D., Dana-Farber Cancer Institute, 450 Brookline Avenue, LC 3216, Boston, MA 02215, Phone: 617-632-6307, Fax: 617-582-8240, loren_walensky@dfci.harvard.edu. Joseph T. Opferman, Ph.D., St. Jude Children's Research Hospital, 262 Danny Thomas Place, Memphis, TN 38105, Phone: 901-595-5524, Fax: 901-525-8025, Joseph.Opferman@stjude.org.

[6]Lead Contact

AUTHOR CONTRIBUTIONS

S.E. and L.D.W conceived of and designed the study. S.E. performed SAHB pull-downs, proteomic analyses, binding studies, *in vitro* enzyme activity assays, and acylcarnitine quantification in MEFs and liver. S.E. and E.B.C conducted the crosslinking experiments. S.L. assisted in the analysis of the proteomics and crosslinking data sets, and executed the HXMS experiments with T.E.W. under the guidance of J.R.E. R.M. and G.H.B synthesized SAHB peptides. A.M.M. assisted S.E. with recombinant VLCAD production and characterization. J.L. performed the docking calculations. S.E and E.Z. designed the FAO experiments and E.Z. performed these studies under the guidance of M.C.H. C.P.M. and J.T.O. conceived of and performed the murine proteomics analysis, including the generation of MEF lines and murine models. J.C. carried out the gene set enrichment analysis studies under the guidance of U.S. L.D.W. and S.E. wrote the manuscript, which was edited and reviewed by all co-authors.

DECLARATION OF INTERESTS

L.D.W. is a scientific advisory board member and consultant for Aileron Therapeutics. L.D.W. and S.E. have a patent filing related to this work.

(BH3) α-helix of MCL-1 can directly engage very long-chain acyl-CoA dehydrogenase (VLCAD), a key enzyme of the mitochondrial fatty acid β-oxidation (FAO) pathway. Proteomic analysis confirmed that the mitochondrial matrix isoform of MCL-1 (MCL-1^{Matrix}) interacts with VLCAD. *Mcl-1* deletion, or eliminating MCL-1^{Matrix} alone, selectively deregulated long-chain FAO, causing increased flux through the pathway in response to nutrient deprivation. Transient elevation in MCL-1 upon serum withdrawal, a striking increase in MCL-1 BH3/VLCAD interaction upon palmitic-acid titration, and direct modulation of enzymatic activity by the MCL-1 BH3 α-helix are consistent with dynamic regulation. Thus, the MCL-1 BH3 interaction with VLCAD revealed a separable, gain-of-function role for MCL-1 in the regulation of lipid metabolism.

eTOC SUMMARY

MCL-1 is a formidable BCL-2 family protein implicated in human cancer and its genetic deletion causes profound physiologic consequences not compensated for by anti-apoptotic homologs. Escudero et al. report that the MCL-1 BH3 α-helix directly binds to and modulates VLCAD, revealing a new role for MCL-1 in regulating lipid metabolism.

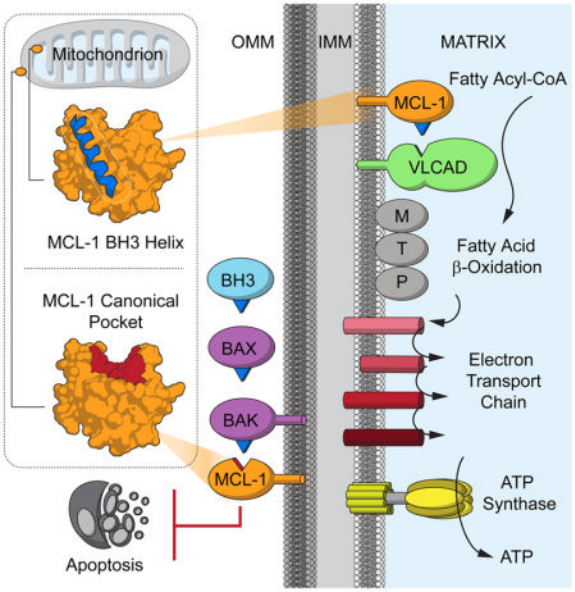

Keywords

MCL-1; BCL-2 family; apoptosis; mitochondria; mitochondrial matrix; VLCAD; fatty acid metabolism; β-oxidation; stapled peptide; α-helix

INTRODUCTION

Mitochondrial apoptosis is essential to normal development and tissue homeostasis (Danial and Korsmeyer, 2004). BCL-2 family proteins regulate this process through heterodimeric and homo-oligomeric protein interactions, which ultimately dictate whether a cell will live or die (Youle and Strasser, 2008). The founding member of the family, BCL-2, was

discovered at the t(14;18) chromosomal breakpoint in follicular lymphoma (Tsujimoto et al., 1984) and revealed that, in addition to a hyperproliferative aberration, cancer cells could be driven by a blockade in the natural cell death pathway. Since then, an entire family of BCL-2 proteins has emerged, whose members have been classified based on the presence of conserved BCL-2 homology (BH) domains and their functionalities (Danial and Korsmeyer, 2004; Youle and Strasser, 2008). Engagement of multidomain pro-apoptotic members BAX and BAK by select BH3-only proteins, such as BID, BIM and PUMA, conformationally activates BAX and BAK, transforming them from monomeric proteins into oligomeric pores that pierce the mitochondrial outer membrane, resulting in apoptosis induction (Walensky and Gavathiotis, 2011). Anti-apoptotic proteins, such as BCL-2 and MCL-1, bind and block BH3-only and multidomain pro-apoptotic members to prevent mitochondrial apoptosis (Cheng et al., 2001). Cancer cells overexpress BCL-2 family anti-apoptotic proteins to exploit this mechanism and enforce cellular immortality, prompting the development of selective BCL-2 and MCL-1 inhibitors such as the FDA-approved drug venetoclax (Souers et al., 2013) and the prototype agent S63845 (Kotschy et al., 2016), respectively.

In addition to their canonical roles in regulating apoptosis, select BCL-2 family proteins have been shown to have essential functions in homeostatic pathways, including mitochondrial morphogenesis (BAX/BAK) (Karbowski et al., 2006), glucose-stimulated insulin secretion (BAD) (Danial et al., 2003), and the DNA damage response (BID) (Kamer et al., 2005; Zinkel et al., 2005). The striking phenotypes of mice with global and tissue-specific *Mcl-1* deletion also point to broader physiologic roles for MCL-1. For example, *Mcl-1*$^{-/-}$ mice exhibit embryonic lethality due to failed implantation, a defect not compensated for by any other BCL-2 family homolog (Rinkenberger et al., 2000). Conditional deletion of *Mcl-1* in B- and T-cells triggers their rapid loss and immune deregulation (Opferman et al., 2003), whereas bone marrow targeting results in hematopoietic stem cell loss and profound, fatal anemia (Opferman et al., 2005). Recently, loss of a mitochondrial matrix isoform of MCL-1 was found to disrupt mitochondrial morphology, mitochondrial fusion, and ATP production (Perciavalle et al., 2012), with conditional *Mcl-1* deletion in cardiomyocytes leading to a rapidly fatal dilated cardiomyopathy (Wang et al., 2013). Notably, the mitochondrial abnormalities observed in cardiomyocytes were not rescued by deletion of the pro-apoptotic effectors BAX and BAK, indicative of a potential non-apoptotic role for MCL-1 in mitochondrial physiology. However, the mechanistic basis for such MCL-1-related phenomena remain unknown.

Anti-apoptotic BCL-2 family proteins manifest differential binding specificities for their pro-apoptotic targets, with MCL-1 having a distinct interaction profile from its homologs BCL-2, BCL-X_L, and BCL-w (Certo et al., 2006). To elucidate the molecular determinants for MCL-1 selectivity, we previously undertook a screening analysis of the MCL-1 binding propensities of all natural BH3 domain helices, generated as stapled peptides named stabilized alpha-helices of BCL-2 domains (SAHBs). We discovered that the MCL-1 BH3 helix, previously known only for its structural, hydrophobic contribution to the surface groove that traps the BH3 domain helices of pro-apoptotic members, was itself the only exclusive inhibitor of MCL-1 (Stewart et al., 2010). This unexpected result suggested that a conformationally-exposed MCL-1 BH3 helix could potentially serve as a mediator of protein interaction, perhaps similar to how exposure of the BAX and BAK BH3 helices upon

apoptosis induction makes these critical domains accessible for either auto-interaction or anti-apoptotic entrapment (Sattler et al., 1997; Walensky and Gavathiotis, 2011).

Given (1) the unique and unexplained phenotypes of MCL-1-deficient cells and tissues, (2) the role of pro-apoptotic BH3 domains as critical BCL-2 family interaction motifs, and (3) our discovery that the BH3 domain of anti-apoptotic MCL-1 is capable of binding as a ligand via its hydrophobic surface, we undertook an exploratory proteomic analysis to uncover potential targets of the MCL-1 BH3 helix. Here, we discovered that the MCL-1 BH3 α-helix directly interacts with very long-chain acyl-CoA dehydrogenase (VLCAD), a key enzyme of the mitochondrial fatty acid β-oxidation pathway, revealing a functional role for MCL-1 in the dynamic regulation of lipid metabolism.

RESULTS

Identification of VLCAD as a Target of the MCL-1 BH3 Helix

An N-terminally biotinylated SAHB designed based on the MCL-1 BH3 sequence (Btn-MCL-1 SAHB$_D$) was applied in a proteomics workflow employing wild-type mouse embryonic fibroblast (MEF) lysates and high-stringency streptavidin capture (Figure 1A, Table S1). Using optimized peptide input and wash conditions, we first confirmed selective capture of endogenous MCL-1 protein by Btn-MCL-1 SAHB$_D$ as compared to vehicle control (Figures S1A–C). Streptavidin bead eluates were then subjected to SDS-PAGE electrophoresis, Coomassie staining (Figure S1D), and in-gel digestion for mass spectrometry analysis. An average of 1,576 versus 384 proteins were identified in Btn-MCL-1 SAHB$_D$ and vehicle eluates (Figure S1E), respectively, and to merit further consideration, peptide-bound proteins were required to have at least 2 spectral counts and a CRAPome (Mellacheruvu et al., 2013) frequency of less than 10%. Fold-enrichment in Btn-MCL-1 SAHB$_D$ versus vehicle eluates, and p value analysis of the data over three biological replicates, identified high-confidence MCL-1 BH3 interactors with Benjamini-Hochberg FDR of <0.02 and fold-enrichment of >6 (Figure 1B, Table S2). Given the recent identification of a mitochondrial matrix isoform of MCL-1 (MCL-1^{Matrix}) and its effect on mitochondrial respiration (Perciavalle et al., 2012), we were particularly interested in potential binding partners whose function resided in the mitochondrial matrix. Of the 49 candidates that met our high stringency criteria, only one was a matrix-resident protein, namely VLCAD, which demonstrated an average spectral count of 27 in MCL-1 SAHB$_D$ pull-downs compared to 0 for the corresponding vehicle control samples, and 49% sequence coverage (Figure 1C, Table S2).

To validate VLCAD as a specific hit, we repeated the streptavidin pull-down experiments using MEF lysates and a series of SAHBs representing the diverse sequence compositions of MCL-1, BIM, BID, and BAD BH3 domains (Figure 1D). Whereas the SAHB panel faithfully recapitulated the physiologic binding selectivities of BH3 domains for MCL-1 interaction, only MCL-1 SAHB$_D$ pulled down endogenous VLCAD (Figure 1D). To rule out a sequence-independent role for the MCL-1 SAHB$_D$ pull-down based on its distinct staple location, we confirmed that an MCL-1 SAHB bearing an all-hydrocarbon staple in the “A” position (flanking the conserved I/V/M-G-D motif) found in the BIM, BID, and BAD constructs also engaged VLCAD, whereas a BIM SAHB bearing a staple in the same

position as MCL-1 SAHB$_D$ (flanking R-N-H in MCL-1 and A-Y-Y in BIM) did not pull down VLCAD (Figure S2). We further found that MCL-1 SAHB$_D$ selectively bound to VLCAD but not to other members of the acyl-CoA dehydrogenase family, such as MCAD and SCAD (Figures 1E, S1F–G). Finally, in advance of drilling down on the binding determinants of the interaction and its mechanistic role, we confirmed by proteomic analysis that FLAG-MCL-1 (full-length protein), reconstituted into *Mcl-1*$^{-/-}$ murine livers, also pulled down native VLCAD and established physiologic interactors of MCL-1, such as BIM and PUMA, and not MCAD or SCAD (Figure 1F). This selective VLCAD interaction profile, obtained using MCL-1 protein and MCL-1 SAHB$_D$, further validated the fidelity of a stapled peptide α-helix as a proteomic discovery tool.

Biochemical Characterization of the MCL-1 BH3/VLCAD Interaction

To dissect a mechanistic role for MCL-1 in regulating VLCAD, we first conducted a series of binding assays to evaluate whether or not the BH3 interaction was direct. We generated full-length, recombinant VLCAD protein (Figure 2A) and indeed found that Btn-MCL-1 SAHB$_D$ directly engaged recombinant VLCAD, whereas BIM, BID and BAD SAHBs showed little to no VLCAD interaction but recapitulated their MCL-1 binding selectivities, as assessed by streptavidin pull-down (Figure 2B). Then, using two additional and distinct methods, ^{19}F-NMR and biolayer interferometry (BLI), we observed direct binding interactions of MCL-1 SAHB$_D$ with both recombinant VLCAD and MCL-1ΔNΔC (Figures 2C–F, S3). As a measure of binding specificity, an MCL-1 SAHB bearing a staple in the “B” position (flanking residues T-L-R in MCL-1), which was found to disrupt the interaction with VLCAD but not MCL-1 in streptavidin pull-downs from MEF lysates (Figure S2), recapitulated this selective binding profile in both ^{19}F-NMR and BLI analyses (Figures 2C–F, S3).

We next investigated the binding determinants for the MCL-1 BH3/VLCAD interaction by generating a series of Btn-MCL-1 SAHB$_D$ alanine point mutants and performing streptavidin pull-downs from MEF lysates. In comparing the binding activities toward native VLCAD and MCL-1, we observed a series of alanine mutants that disrupted both binding interactions, but also identified residues that revealed selectivity for each of the targets (Figure 3A–B, Table S1). For example, mutagenesis of L213 - a conserved residue across all BH3 domains – disrupted Btn-MCL-1 SAHB$_D$ interaction with VLCAD and MCL-1, whereas alanine mutation of L210 or the previously identified MCL-1 selectivity determinant V220 (Stewart et al., 2010) were uniquely disruptive to VLCAD and MCL-1, respectively. Most striking, the series of disruptive mutations for each target defined partially overlapping binding interfaces that were shifted from one another by approximately 90 degrees (Figures 3A–B), revealing a distinct mode for MCL-1 BH3 interaction with VLCAD.

MCL-1 SAHB$_D$ Engages a Surface Groove Near the Active Site of VLCAD

To localize the region of MCL-1 BH3 interaction on VLCAD, we applied a photoaffinity labeling mass spectrometry approach using a panel of photoreactive SAHB (pSAHB) peptides bearing a benzophenone moiety, and capped with biotin at the N-terminus (Braun et al., 2010). Each pSAHB was incubated with recombinant VLCAD under UV light, and the

peptide fragments that covalently linked to the pSAHB via the benzophenone were identified by liquid chromatography-tandem mass spectrometry (LC-MS/MS). Whereas MCL-1 pSAHBs *D1* and *D2* both crosslinked to VLCAD residues V292 and M294, MCL-1 pSAHB$_{D2}$ also captured amino acids T240, F242, R246, and G250, and MCL-1 pSAHB$_{D3}$ crosslinked to S32, F38, and S445 (Figure 4A). Intriguingly, the series of identified crosslinks all localized to a discrete surface groove formed by α-helices that comprise the defined α-helical 2 domain of VLCAD (McAndrew et al., 2008) and lie just proximal to the binding sites of the FAD co-factor and the enzymatic substrate itself (Figure 4B). Using the identified crosslinks as constraints for computational docking, the MCL-1 BH3 motif is predicted to engage VLCAD by a helix-in-groove interaction that is analogous to the interaction paradigm for BH3 helices with BCL-2 family anti-apoptotic pockets (Sattler et al., 1997; Stewart et al., 2010) (Figure 4B).

To validate these findings by a distinct methodology, we undertook hydrogen-deuterium exchange mass spectrometry (HXMS) analysis of the interaction between recombinant VLCAD and the VLCAD-selective MCL-1 SAHB$_D$ V220A construct. HXMS probes protein structure by measuring both the solvent accessibility and hydrogen-bonding states of backbone amide hydrogens (Engen, 2009). When diluted into deuterium buffer, backbone hydrogens of flexible and/or exposed protein regions rapidly exchange with deuterium, whereas buried domains, regions that contain hydrogen bonding involving backbone amide hydrogens (such as those in α-helices), and/or residues that become engaged by ligand interaction, demonstrate a slowed or suppressed deuterium exchange. Here, we observed protection of peptide fragments encompassing residues 431–489 of VLCAD upon MCL-1 SAHB interaction (Figure 4C–D). This discrete region, which includes a flexible loop, overlaps with and is in the immediate vicinity of those residues crosslinked by MCL-1 pSAHB$_{D3}$ at the base of the surface groove, further validating the photoaffinity labeling results. Taken together, the diversity of binding studies (Figures 1–2, S3), and the alanine scanning (Figure 3A–B), photoaffinity labeling (Figure 4A–B), and HXMS (Figure 4C–D) analyses reveal the first example of a BH3 domain helix from an anti-apoptotic BCL-2 family member serving as a ligand for protein interaction.

Deregulation of Fatty Acid Oxidation upon *Mcl-1* Deletion is Isoform Specific

To examine the functional relevance of the identified MCL-1 BH3/VLCAD interaction, we first tested the impact of chronic and acute deletion of *Mcl-1* on long-chain fatty acid β-oxidation in MEFs exposed to supplemental palmitic acid. Comparing wild-type and *Mcl-1*$^{-/-}$ MEFs, we observed relative elevation of long-chain fatty acylcarnitines by mass spectrometry analysis (Figure 5A). We then repeated the analysis upon conditional deletion of *Mcl-1* using *Mcl-1*$^{fl/fl}$CreER^{T2} MEFs (Perciavalle et al., 2012) (Figure S4), comparing vehicle- and tamoxifen-treated cells. The results were strikingly similar, indicating that an acute or chronic absence of MCL-1 leads to elevation of the very substrate precursors of VLCAD (Figure 5B). To validate these findings in an *in vivo* context, we compared fatty acylcarnitine levels in *Mcl-1*-deleted murine livers with or without reconstitution of wild-type MCL-1. Consistent with our findings in MEFs, we observe relative elevation of long-chain fatty acylcarnitines in *Mcl-1*-deleted murine livers and reduction of levels upon reconstitution with MCL-1 (Figure 5C). We next sought to evaluate whether the observed

increase in long-chain fatty acylcarnitine levels could be explicitly linked to the recently described mitochondrial matrix isoform of MCL-1, MCL-1^{Matrix} (Perciavalle et al., 2012). To accomplish this goal, we performed comparative acylcarnitine analyses on a series of MEFs with differential levels of outer mitochondrial membrane (OMM) and matrix forms of MCL-1 (Perciavalle et al., 2012) (Figure 5D–E). Interestingly, the level of observed long-chain fatty acylcarnitine accumulation was inversely correlated to the cumulative amount of native and/or expressed MCL-1^{Matrix}, but was unaffected by the presence or absence of MCL-1^{OMM} (Figure 5F).

With these data having implicated MCL-1^{Matrix} as the candidate MCL-1 isoform for VLCAD regulation, we sought to confirm an isoform-specific interaction *in vivo*. Therefore, we repeated the murine liver proteomic analysis, but this time reconstituted *Mcl-1*$^{-/-}$ livers with FLAG-MCL-1^{OMM} or FLAG-MCL-1^{Matrix}. In comparison with the FLAG-MCL-1 wild-type pull-down (both forms present) (Figure 1F), we observed selective enrichment for VLCAD in the FLAG-MCL-1^{Matrix} pull-down, whereas the BH3-only protein targets BIM and PUMA were enriched in the FLAG-MCL-1^{OMM} pull-down (Figure 5G). To rule out the possibility that the interaction between VLCAD and FLAG-MCL-1^{Matrix} was non-specifically enriched due to matrix targeting of the reconstituted protein (despite the compartment-independent re-equilibration of protein interactions that can occur after tissue lysis), we assessed the selectivity of VLCAD interaction in comparison with another CAD of equal abundance, as determined by a compiled proteomics database (Wang et al., 2015), namely LCAD (Figure S5A). We found that, despite their similar abundance, there was a striking 10-fold enrichment of VLCAD in the FLAG-MCL-1^{Matrix} pull-down compared to LCAD, highlighting the selectivity of interaction (Figure S5B). Exemplary mitochondrial proteins of varying abundance with no structural relationship to VLCAD likewise showed no non-specific enrichment for FLAG-MCL-1^{Matrix} as compared to the GFP control (Figure S5). Taken together, the acylcarnitine and proteomic data point to a specific role for MCL-1^{Matrix} in regulating fatty acid β-oxidation through VLCAD interaction.

Increased Long-Chain Fatty Acid Oxidative Flux in the Absence of MCL-1^{Matrix}

Whereas the acylcarnitine data pointed to a role for MCL-1^{Matrix} in regulating fatty acid β-oxidation, the observed elevations could reflect either accumulation from impaired VLCAD activity or enhanced mobilization due to increased flux through the pathway. To distinguish between these mechanistic possibilities, we directly measured β-oxidation of ^{3}H-palmitic acid in our panel of MEFs. In addition, we included ^{3}H-hexanoic acid in the analyses to evaluate chain-length specificity, and compared fatty acid oxidation rates in the presence and absence of serum to probe for context-dependent dynamic regulation. As expected, serum deprivation of cultured wild-type MEFs resulted in a boost in ^{3}H-palmitic acid oxidation. Whereas chronic *Mcl-1*$^{-/-}$ deletion had no effect on the relative level of ^{3}H-palmitic acid oxidation in the homeostatic, serum-containing state, the absence of MCL-1 resulted in a statistically significant elevation in ^{3}H-palmitic acid oxidation in the serum-starved condition (Figure 6A). Importantly, no such difference was observed for ^{3}H-hexanoic acid oxidation (Figure 6B), highlighting a specific link between *Mcl-1* deletion and deregulation of long-chain fatty acid oxidation upon serum deprivation. We repeated the analysis in the context of acute *Mcl-1* deletion and observed similar results (Figure 6C–6D). Next, we

examined whether the selective increase in ^{3}H-palmitic acid oxidation observed under serum-starved conditions could be attributed to the OMM vs. matrix isoforms of MCL-1. We found that in the absence of MCL-1^{Matrix}, but not MCL-1^{OMM}, the relative oxidation rate of ^{3}H-palmitic acid increased (Figure 6E). When the experiment was repeated with ^{3}H-hexanoic acid, no such difference was observed (Figure 6F). The pattern of these findings is consistent with our acylcarnitine analyses that revealed the same deregulated phenotype whether *Mcl-1* deletion was chronic or acute (Figure 5A–B), and specific tracking of the abnormality with the mitochondrial matrix isoform of MCL-1 (Figure 5D–F). From a functional standpoint, the increase in long-chain fatty acid oxidative activity observed upon elimination of MCL-1^{Matrix} suggests that the corresponding elevation of long-chain fatty acylcarnitines in this context reflects increased flux through the pathway.

Given the advancement of small-molecule MCL-1 inhibitors to Phase I clinical testing in cancer, we sought to determine if a prototype inhibitor such as S63845 could also influence long-chain fatty acid oxidation. S63845 is a BH3 mimetic compound that selectively targets the surface groove of MCL-1 (Kotschy et al., 2016). Since loss-of-function mutation of the MCL-1 groove did not alter the mitochondrial phenotype associated with MCL-1^{Matrix} in reconstituted cells (Perciavalle et al., 2012), and the interaction between the hydrophobic face of MCL-1 BH3 and VLCAD (Figures 3–4) implies an altered MCL-1 conformation, we hypothesized that S63845 would have no effect on long-chain fatty acid oxidation. Indeed, we found that treatment of wild-type MEFs with S63845 under serum-starved conditions did not alter the rate of ^{3}H-palmitic acid oxidation (Figure 6G). This result is consistent with a lack of overt toxicity, including cardiotoxicity (Wang et al., 2013), in S63845-treated mice (Kotschy et al., 2016), which might otherwise be adversely affected if the compound's spectrum of MCL-1 inhibition included MCL-1^{Matrix}.

Dynamic Regulation of MCL-1 and its Functional Interaction with VLCAD

The selective effect of eliminating MCL-1^{Matrix} on ^{3}H-palmitic acid oxidation and long-chain fatty acylcarnitine levels under conditions of heightened fatty acid oxidative flux (serum deprivation or palmitic acid supplementation) suggested that the observed regulation was dynamic. To test this hypothesis, we monitored MCL-1 protein levels in wild-type MEFs upon serum withdrawal. Interestingly, we observed a notable increase in MCL-1 protein within 15 minutes of eliminating serum, with peak levels achieved by approximately 1–3 hours (Figure 6H). Given the challenge of trapping dynamic and context-dependent native-protein interactions by co-immunoprecipitation after cell lysis, we explored the direct interaction between the MCL-1 BH3 helix and recombinant VLCAD under conditions of increased palmitoyl-CoA concentrations. Streptavidin pull-downs of biotinylated MCL-1 SAHB$_{D}$ upon palmitoyl-CoA titration yielded a striking increase in VLCAD co-precipitation that directly correlated with palmitoyl-CoA level, as monitored by electrophoresis and Coomassie stain (Figure 6I). In contrast, the addition of hexanoyl-CoA at the identical dosing had no effect on the baseline level of MCL-1 SAHB$_{D}$/VLCAD co-precipitation (Figure 6I).

In an effort to link the metabolic consequences of eliminating MCL-1^{Matrix} (Figure 6A–F) and the observed substrate-dependent enhancement of MCL-1 SAHB$_{D}$/VLCAD interaction

(Figure 6I) to a direct functional effect on enzymatic activity, we monitored long-chain fatty acid oxidation by recombinant VLCAD in the presence and absence of MCL-1 SAHBs. In the presence of the most potent VLCAD interactor, MCL-1 SAHB$_D$ D218A (Figure 3A), we detected inhibition of VLCAD-mediated palmitic acid oxidation, as reflected by a statistically-significant decrease in the enzyme's initial velocity, V_0 (Figure 6J–K). Importantly, little to no effect was observed upon MCL-1 SAHB$_D$ R215A mutagenesis, which essentially abrogates VLCAD-binding activity (Figure 3A), highlighting the sequence-dependence of the inhibitory effect. Taken together, these data suggest that the MCL-1 BH3 helix can directly modulate the enzymatic activity of VLCAD, with the observed *in vitro* suppressive effect consistent with the heightened activity of long-chain fatty acid oxidation observed in MEFs upon selective elimination of the mitochondrial matrix isoform of MCL-1.

A Link Between Pathologic MCL-1 Expression and Fatty Acid Metabolism in Cancer

Given MCL-1's prominent pathologic role in driving the apoptotic resistance of human cancer, we explored whether a second function in regulating fatty acid metabolism segregates with MCL-1 expression level in the context of oncogenic stress. We examined two independent datasets containing 524 and 294 cases of acute myeloblastic leukemia (AML) (Valk et al., 2004; Wouters et al., 2009), parsing MCL-1 expression level by quartile and then exploring correlations with metabolic signatures. In each case, gene set enrichment analysis revealed a statistically significant correlation between elevated MCL-1 expression and a fatty acid β-oxidation signature (Figure 7A–B). Importantly, when the identical analysis was performed with an alternate anti-apoptotic BCL-2 family protein, such as BCL-X_L, no such correlation was observed (Figure 7C–D). Thus, in the context of two pathophysiologic states, nutrient deprivation (Figure 6) and cancer (Figure 7), we find an unexpected link between MCL-1 and fatty acid β-oxidation.

DISCUSSION

BCL-2 family BH3 motifs are evolutionarily conserved protein interaction modules with potentially diverse targets and functionalities beyond their canonical interactions with pro- and anti-apoptotic proteins at the mitochondria (Aouacheria et al., 2015). Here, we discovered by a combination of proteomic, biochemical, and binding site analyses that the MCL-1 BH3 α-helix directly binds to and influences the enzymatic activity of VLCAD. Alanine mutagenesis localized the critical binding determinants to a portion of the hydrophobic face that overlaps with, but is distinct from, the MCL-1 BH3-binding interface implicated in auto-interaction (Stewart et al., 2010). Functional analyses, spanning acute and chronic *Mcl-1* deletion, and MCL-1 reconstitution scenarios in MEFs and murine livers, revealed that MCL-1 modulates long-chain fatty acid β-oxidation. Specifically, our data collectively suggest that MCL-1^{Matrix} participates in the dynamic regulation of VLCAD activity during physiologic stress, potentially constraining "runaway" enzymatic activity. Thus, we report the first example of a gain-of-function role for an anti-apoptotic BH3 domain, with the MCL-1 BH3 helix itself serving as a ligand for protein interaction with a non-canonical BCL-2 family target. With the identification of glucokinase (Danial et al., 2003; Danial et al., 2008) and now VLCAD as metabolic enzymes subject to regulation by

the pro-apoptotic BH3 domain of BAD and anti-apoptotic BH3 domain of MCL-1, respectively, a biological theme of BCL-2 family proteins functioning at the crossroads of mitochondrial apoptosis and metabolism is emerging.

This study was motivated by the complexity of phenotypes associated with the MCL-1 protein, including observed physiologic defects not compensated for by the multitude of anti-apoptotic BCL-2 homologs upon *Mcl-1* deletion (Opferman et al., 2005; Opferman et al., 2003; Rinkenberger et al., 2000; Wang et al., 2013). What's more, the recent discovery of a mitochondrial matrix isoform of MCL-1, whose apparent metabolic function was not impaired by disruption of the canonical BH3-binding groove of MCL-1, suggested a distinctive structure-function mechanism for this post-translationally truncated isoform (Perciavalle et al., 2012). Our previous discovery that the anti-apoptotic MCL-1 BH3 helix could function as a ligand in a manner previously ascribed only to pro-apoptotic BH3 helices (Stewart et al., 2010) suggested the possibility that a distinct conformation of MCL-1 - in which the BH3 helix is exposed - could underlie alternative protein interaction mechanisms. We have used structurally reinforced "stapled" BH3 helices to recapitulate and probe the natural biological activity of these critical domains, including deploying them to locate binding sites on interacting targets (Braun et al., 2010; Walensky and Bird, 2014). Here, we converted the stapled MCL-1 BH3 helix into a proteomic discovery tool that identified VLCAD as the only interacting protein located in the mitochondrial matrix. Indeed, the corroboration between MCL-1 $SAHB_D$ and expressed full-length MCL-1 protein, and $MCL\text{-}1^{Matrix}$ in particular, in engaging VLCAD indicates that stapled peptide helices can serve as high-fidelity proteomic tools to uncover and catalog the protein targets of structured interaction motifs. From a biomedical perspective, our results indicate that the functionalities, interaction paradigms, and druggable mechanisms of BCL-2 family proteins may extend well beyond their renowned roles as control points for apoptotic regulation.

The unexpected link between MCL-1 and VLCAD potentially provides a unifying mechanism for phenotypic outcomes shared by the two proteins. For example, conditional deletion of *Mcl-1* or *Acadvl* (VLCAD) in murine cardiomyocytes leads to dilated cardiomyopathy (Wang et al., 2013; Xiong et al., 2014), which is also seen in children with the severe form of VLCAD deficiency (Strauss et al., 1995). VLCAD is bound to the inner mitochondrial membrane and catalyzes the first of four steps of fatty acid β-oxidation, dehydrogenating the C2–C3 bond of fatty acyl-CoA chains containing 14–20 carbons. The pathway is critical to converting the energy stored in fats into ATP, with the heart relying on fatty acids as the preferred substrate for ATP production. The cardiac damage sustained as a result of VLCAD deficiency derives both from energy depletion and toxicity from the accumulated long-chain fatty acids and carnitine derivatives (Wajner and Amaral, 2015). Lipotoxicity can induce mitochondrial dysfunction that manifests as altered mitochondrial morphology, bioenergetic imbalance, and decreased mitochondrial membrane potential. Proteolytic processing of the MCL-1 amino terminus upon mitochondrial import yields a 36 kD isoform that, like VLCAD, is tethered to the inner mitochondrial membrane and exposed to the matrix (Perciavalle et al., 2012). In the absence of the mitochondrial matrix isoform of MCL-1, mitochondrial morphology, ATP production, and membrane potential are disrupted (Perciavalle et al., 2012). Here, we find that, in contrast to VLCAD deficiency, the absence of $MCL\text{-}1^{Matrix}$ results in hyperactivity of β-oxidation of long-chain fatty acids, which may

also be detrimental due to substrate overconsumption and/or co-factor depletion. Elevated acetyl-CoA levels can likewise induce mitochondrial protein acetylation and loss-of-function (Baeza et al., 2016). Intriguingly, our structural analyses place the MCL-1 BH3 helix in direct proximity to the enzyme active site and adjacent to an unstructured region thought to tether VLCAD to the inner mitochondrial membrane (McAndrew et al., 2008). Thus, it is tempting to speculate that the phenotypic overlap in mitochondrial dysfunction and cardiac pathology observed for VLCAD and MCL-1 deficiencies may be driven, at least in part, by a role for MCL-1^{Matrix} in tuning VLCAD activity.

Recent data suggests that, like cardiomyocytes, cancer cells can also be highly reliant on β-oxidation of fatty acids, but in this case for survival, proliferation, and metastasis (Caro et al., 2012; German et al., 2016; Pascual et al., 2017). Although the pathologic metabolic reprogramming of cancer cells is typically attributed to the Warburg effect and glutamine addiction (DeBerardinis et al., 2007; Smith et al., 2016), fatty acid β-oxidation has recently been shown to promote leukemic growth, with pharmacologic blockade of the pathway especially cytotoxic *in vitro* and *in vivo* (German et al., 2016; Samudio et al., 2010). A subset of diffuse large B-cell lymphomas (DLBCLs) that manifest an oxidative phosphorylation (OXPHOS) gene expression signature oxidize fatty acids at higher rates than other DLBCL subtypes, and depend on β-oxidation for survival and growth (Caro et al., 2012). In human oral carcinomas, a robust lipid metabolism gene signature has been linked to high metastatic potential (Pascual et al., 2017). Intriguingly, MCL-1 is the most common anti-apoptotic driver across all human cancers (Beroukhim et al., 2010), yet this preference for MCL-1 among BCL-2 family homologs is largely unexplained. Here, we found increased MCL-1 BH3/VLCAD binding activity upon exposure to elevated palmitoyl-CoA levels, acute elevation of MCL-1 protein levels upon serum withdrawal, and aberrantly elevated long-chain fatty acid flux in the absence of MCL-1^{Matrix} under serum-starved conditions, all linking MCL-1 to dynamic modulation of long-chain fatty acid β-oxidation. We further identified statistically significant correlations between elevated levels of MCL-1 expression and a fatty acid oxidation signature in human AML. Dual roles for MCL-1 in apoptotic suppression by the OMM form, and control of fatty acid β-oxidation by the matrix form in response to stress, could underlie the oncogenic supremacy of MCL-1. Interestingly, recent studies implicated a collaboration between MCL-1 and MYC in regulating OXPHOS activity, which promoted chemoresistance of cancer stem cells in triple-negative breast cancer (Lee et al., 2017). Indeed, blocking cell death and ensuring sustained energy production to support cancer cell proliferation, metastasis, and chemoresistance represents a formidable combination. Whereas small-molecule inhibitors of the MCL-1 groove effectively neutralize its pathologic anti-apoptotic functionality in cancer, targeting the distinct interaction between MCL-1^{Matrix} and VLCAD may provide a therapeutic opportunity to disrupt cancer metabolism by deregulating long-chain fatty acid β-oxidation.

STAR METHODS

CONTACT FOR REAGENT AND RESOURCE SHARING

Further information and requests for resources and reagents should be directed to and will be fulfilled by the Lead Contact, Loren D. Walensky (loren_walensky@dfci.harvard.edu).

EXPERIMENTAL MODEL AND SUBJECT DETAILS

Mice—*Mcl-1*$^{fl/fl}$ mice were generated by targeting *loxP* sites upstream of the start codon and in between exons 1 and 2 of *Mcl-1.* The *Mcl-1*^{fl} allele was then carried through the germline to generate viable *Mcl-1*$^{fl/fl}$ mice (Opferman et al., 2003). To generate mice expressing various forms of MCL-1, *Mcl-1*$^{fl/fl}$ mice were intravenously injected via tail vein with self-complementary adeno-associated virus serotype 8 (scAAV8) vectors packaged by the St. Jude Children's Research Hospital Vector Production Core laboratory. Mice were co-injected with scAAV8-LP1-Cre to delete endogenous *Mcl-1* in the liver (2×10^{11} genome copies per mouse) and one of the following constructs (5×10^{10} genome copies per mouse): scAAV8-LP1-GFP (control), scAAV8-LP1-*Mcl-1*$^{WT;IntFLAG}$ (wild-type MCL-1 construct with an internal FLAG tag that is capable of generating both OMM and Matrix isoforms), scAAV8-LP1-*Mcl-1*$^{OMM;IntFLAG}$ (mutant MCL-1 construct with an internal FLAG tag that only generates the OMM isoform), or scAAV8-LP1- *Mcl-1*$^{Matrix;IntFLAG}$ (mutant MCL-1 construct with an internal FLAG tag that only generates the Matrix isoform). The internal FLAG tag was placed at residue 134 in all three MCL-1 constructs. *Mcl-1*^{OMM} replaces R5 and R6 with alanines. *Mcl1*^{Matrix} is a fusion construct where the N-terminal 50 amino acids of *Neurospora crasa* ATP synthase is fused to the N-terminus of *Mcl-1*$^{\Delta N}$ (deletion of the first 67 amino acids of MCL-1).

Mice were housed in a pathogen-free animal facility at 22°C with a 12 hour light/dark cycle and fed normal chow *ad libitum*. All mice were 6–8 weeks of age and housed in groups of 4–5. Animals harvested for proteomics analysis were a 50:50 mix of males and females, while animals harvested for acylcarnitine analyses were male. Mice were euthanized by CO_2 asphyxiation, and tissues immediately dissected and flash frozen in liquid nitrogen. Tissues were stored at −80°C until further analysis. All mice were bred and utilized in accordance with St. Jude Children's Research Hospital (SJCRH) Animal Care and Use Committee approved protocols.

Microbe Strains—Recombinant proteins were expressed in BL21(DE3) *E. coli*, which were grown in Luria Broth (LB) at 37°C with shaking at 220 rpm.

Cell Lines—SV40-transformed wild-type, *Mcl-1*$^{-/-}$, *Mcl-1*$^{+/+}$ Rosa-ERCre^{T2}, *Mcl-1*$^{fl/fl}$ Rosa-ERCre^{T2}, *Mcl-1*$^{fl/fl}$ Rosa-ERCre^{T2} + MCL-1^{OMM}, and *Mcl-1*$^{fl/fl}$ Rosa-ERCre^{T2} + MCL-1^{Matrix} mouse embryonic fibroblasts (MEFs) were maintained at 37°C in Dulbecco's modified Eagle's medium (DMEM) (Invitrogen) supplemented with 10% (v/v) fetal bovine serum, 100 U/ml penicillin/streptomycin, and 2 mM glutamine following standard culture conditions and procedures. To induce Cre expression, cells were treated with 100 nM 4-hydroxytamoxifen (Sigma-Aldrich, Cat# H7904) in media for 48 hours. All cell lines were confirmed to be mycoplasma-free using the MycoAlert^{TM} mycoplasma detection kit (Lonza Biologics Inc., Cat# LT07-218). MEF lines employed in this study were generated, characterized, and previously reported by J.T.O. (Opferman et al., 2003; Perciavalle et al., 2012).

METHOD DETAILS

Stapled Peptide Synthesis—Stapled peptides and their photoreactive analogs were synthesized, derivatized, purified by LC/MS to >95% homogeneity, and quantified as previously described (Bird et al., 2011; Braun et al., 2010). Stapled peptides were generated using solid phase Fmoc chemistry on a Symphony X peptide synthesizer, with amino acids sequentially added to rink amide AM resin (Millipore, Cat# 855120). S-pentenyl alanine non-natural amino acids (Nagase & Co, Cat# 365023) replaced two native amino acids at the *i, i+4* positions. The all-hydrocarbon stapled was formed by olefin metathesis using the Grubbs first-generation ruthenium catalyst (Sigma Aldrich, Cat# 579726), followed by peptide deprotection and cleavage from the resin. Stapled peptides were then purified by reverse phase high performance liquid chromatography and mass spectrometry (LC/MS) and quantified by amino acid analysis. Peptides were N-terminally derivatized with either acetyl, biotin-β-alanine (Advanced ChemTech, Cat#'s FA2601 and RB8575), or biotin-PEG-β-alanine (Millipore, Cat# 851029). For peptides used in ^{19}F NMR studies, phenylalanine residues were replaced with trifluoromethyl-L-phenylalanine (Chem-Impex International Inc., Cat# 07392). Photoreactive stapled peptides were generated by inserting the benzophenone-containing amino acid at the indicated locations (Advanced ChemTech, Cat# FF2424). Stapled peptide compositions, observed masses, and their experimental applications by figure are listed in Table S1.

Streptavidin Capture—Wild-type MEFs were trypsinized, washed once with cold PBS, and lysed on ice with NP-40 lysis buffer (1 mL/10^6 cells; 50 mM Tris, pH 7.4, 150 mM NaCl, 0.5% [v/v] NP-40, complete protease inhibitor pellet [Roche, Cat# 16829800]). Cellular debris was pelleted at 14,000×g for 10 min at 4°C, and protein concentration of the supernatant quantified using the BCA Protein Assay Kit (Thermo Fisher Scientific, Cat# 23225). Lysates (2 mg/pull-down) were pre-cleared by exposure to 50 μL of pre-equilibrated high capacity streptavidin agarose beads (Thermo Fisher Scientific, Cat# PI20359), and then incubated with biotinylated SAHBs (15 nmol) or vehicle (1.5% [v/v] DMSO) overnight at 4°C, followed by addition of 50 μL of pre-equilibrated streptavidin agarose beads for 2 hours at 4°C. The beads were pelleted and washed with NP-40 lysis buffer three times before eluting the protein sample from the beads by heating at 70°C for 10 min in SDS loading buffer. Samples were subjected to electrophoresis, Coomassie staining (SimplyBlue Safe Stain, Thermo Fisher Scientific, Cat# LC6065) for proteomic analysis (see below), and/or western blotting using the following antibodies: MCL-1 (Rockland, Cat# 600-401-394, RRID: AB_2266446; 1:1000 in 3% [w/v] BSA), VLCAD (Thermo Fisher Scientific, Cat# PA5-29959, RRID: AB_2547433; 1:1000 in 1% [w/v] milk/0.1% [v/v] Tween-20), MCAD (Thermo Fisher Scientific, Cat# PA5-27201, RRID: AB_2544677; 1:1000 in 3% [w/v] BSA), and SCAD (Abcam, Cat# ab154823; RRID: AB_2716802; 1:1000 in 3% [w/v] BSA). Streptavidin capture using recombinant proteins (see below) was performed with 5 nmol SAHB and 10 pmol protein in a volume of 500 μL. Streptavidin capture using recombinant VLCAD in the presence of palmitoyl-CoA (Sigma-Aldrich, Cat# P9716) or hexanoyl-CoA (Sigma-Aldrich, Cat# H2012) was performed with 7.2 μM VLCAD, 14.4 μM SAHB, and either 0, 18, 36, or 72 μM acyl-CoA in a final volume of 500 μL. Densitometry analyses were performed using ImageJ software.

Mass Spectrometry Analysis—Each lane of Coomassie-stained gel from the MEF lysate streptavidin-capture samples was divided into 8 sections and further cut into 1 mm × 1 mm cubes. Gel pieces were fully destained in 50% (v/v) acetonitrile/50 mM ammonium bicarbonate at 37°C (~30 min), dehydrated by 3 sequential 5 min soaks in acetonitrile at room temperature, and in-gel trypsin digests performed by submerging the gel pieces in sequencing-grade trypsin (Promega, Cat# V5111) solution at 12.5 ng/μL in 50 mM ammonium bicarbonate for 45 min on ice and then overnight at 37°C. Tryptic peptides were extracted from the gel matrix by submerging the gel pieces in a 50% (v/v) acetonitrile/5% (v/v) formic acid solution twice for 15 min per soak. The resulting extracts were dried by speedvac, purified through C18 OMIX tips according to the manufacturer's instructions (Agilent Technologies, Cat# A57003100), and dried again. Samples were reconstituted in 4 μL of a 5% (v/v) acetonitrile/5% (v/v) formic acid solution and analyzed by LC-MS/MS on a Thermo Orbitrap Discovery XL, as described (Braun et al., 2010). Briefly, peptides were loaded onto a self-packed C4/C18 (100 μm × 25 cm) column using a gradient of 10–40% B (A: 0.125% [v/v] formic acid, 3.1% [v/v] acetonitrile, water; B: 0.125% [v/v] formic acid, acetonitirile). The mass spectrometer was operated in top ten mode with the top 10 most abundant ions from each parent scan subjected to MS/MS. Peptides were identified using both Thermo Protein Discoverer and Xtandem! algorithms, and processed using Scaffold (Proteome Software) with precursor and fragment ion mass tolerances of ± 10.0 ppm and 0.8 Da, respectively. Carbamido-methyl cysteine, oxidized methionine, and phosphorylated serine and tyrosine were set as variable modifications. Protein and peptide thresholds were set to 99% and 95%, respectively. A minimum of two spectral counts and a CRAPome (Mellacheruvu et al., 2013) frequency of less than 10% was used as a threshold for protein hits (Rebsamen et al., 2015). To identify significant interactions, fold-enrichment and p values were calculated after normalizing spectral counts to the number of peptides identified per run, thereby accounting for variations between replicates (Gokce et al., 2011). As a correction for multiple testing, a Benjamini-Hochberg FDR < 0.02 was determined (Diz et al., 2011).

Mouse Liver Proteomic Analysis—Self-complementary adeno-associated virus serotype 8 (scAAV8) vectors expressing Cre recombinase (to delete endogenous *Mcl-1*), GFP, or *Mcl-1* mutants expressing an internal FLAG epitope tag (FLAG-MCL-1) under control of the LP1 liver-specific promoter (Nathwani et al., 2009) were packaged by the SJCRH Vector Production Core laboratory. *Mcl-1*-conditional mice (Opferman et al., 2003) were intravenously injected via tail vein with scAAV-LP1-Cre (2×10^{11} genome copies per mouse) and scAAV-LP1-GFP or scAAV-LP1-FLAG-MCL-1 vectors (5×10^{10} genome copies per mouse). All mice were bred and utilized in accordance with the SJCRH Animal Care and Use Committee approved protocols. Two weeks after viral infection, livers were isolated from euthanized mice and subjected to mitochondrial purification in mito-isolation buffer (200 mM mannitol, 68 mM sucrose, 10 mM HEPES-KOH at pH 7.4, 10 mM KCl, 1 mM EDTA, 1 mM EGTA and 0.1% [w/v] BSA) by differential centrifugation. Mitochondria were further purified using a 70%/30% Percoll gradient (Perciavalle et al., 2012). To assess endogenous MCL-1 deletion and expression of reconstituted MCL-1, immunoblots were performed from lysed liver mitochondria. Frozen isolated mitochondria were subjected to immunoprecipitation with M2 anti-FLAG-agarose beads in a 0.5% (v/v) NP40, 50 mM Tris-

Cl (pH 7.5), 150 mM NaCl buffer containing complete protease inhibitors for 90 min and washed 3 times with the same buffer prior to overnight elution with 200 mg/ml FLAG peptide. Eluted immunoprecipitated samples were run on an SDS-PAGE gel and subjected to tandem mass spectrometry at the SJCRH Proteomics Core Facility. The proteins in the gel bands were reduced with dithiothreitol to break disulfide bonds and the Cys residues were alkylated by iodoacetamide to allow for the recovery of Cys-containing peptides. The gel bands were washed, dried down by speed vacuum, and rehydrated with buffer containing trypsin. Digested samples were acidified, the peptides extracted and loaded onto a nanoscale capillary reverse phase C18 column, and then eluted by a gradient using an HPLC system (Thermo EASY-nLC 1000). The eluted peptides were ionized and detected by an inline mass spectrometer (LTQ Orbitrap Elite). The MS spectra were collected first (in ~0.5 sec) and the top 20 abundant ions were sequentially isolated for MS/MS analysis (each in ~0.1 sec, totaling ~2 sec). This process (~2.5 sec) was cycled over the entire liquid chromatography gradient, acquiring more than 14,000 MS/MS spectra during a 50 min elution. Database searches were performed using the Sequest search engine. All matched MS/MS spectra were filtered by mass accuracy and matching scores to reduce protein false discovery rate (~1%). Each immunoprecipitation was performed from 3 pooled mouse liver preparations and mass spectrometry was performed in duplicate.

Protein Expression—Human VLCAD lacking its cleavable leader sequence (aa 40-655; NCBI: NP_000009.1) was subcloned into the pET19b vector (Millipore, Cat# 69677-3) using NdeI and XhoI restriction sites, and confirmed by DNA sequencing. The His-tagged VLCAD construct was expressed in BL21(DE3) *E.coli* (Invitrogen, Cat# C600003) at 37°C and, upon reaching an optical density (O.D.) of 0.8, bacteria were induced with 0.5 mM isopropylthio-β-galactosidase (IPTG) (Gold Biotechnology, Cat# I2481C) for 4 hours. Bacterial pellets were resuspended in lysis buffer (500 mM NaCl, 50 mM HEPES, 5% glycerol, pH 7.5, complete protease inhibitor tablet) and lysed by microfluidization (M-110L; Microfluidics). Lysates were cleared by centrifugation at 20,000 rpm for 45 min (Beckman Avanti J-E, rotor type JA-20), subjected to Ni-NTA (QIAGEN, Cat# 30230) affinity chromatography, followed by elution with 300 mM imidazole (Sigma-Aldrich, Cat# I2399) and overnight dialysis at 4°C. Dialyzed VLCAD was concentrated and subjected to size exclusion chromatography (GE Healthcare Life Sciences; Superdex 200 10/300 GL) at 4°C using a 150 mM NaCl, 50 mM Tris, pH 8.0 buffer. Protein identification and purity was confirmed by intact mass spectrometry, SDS-PAGE, and VLCAD western blot analysis.

Human VLCADΔEx3, a naturally-occurring splice variant of VLCAD that affords robust recombinant expression (Goetzman et al., 2007) (NCBI: NP_001029031.1), was generated by deleting residues 47–68 from the full-length construct described above using the Q5 Site-Directed Mutagenesis Kit (New England Biolabs, Cat# 23225). The primers used for the PCR reaction were GAGAGCAAAAGCTTCGCCGTTGGCATG and CTGTGCGGCGCCACCGGC. VLCADΔEx3 was expressed and purified as described above.

Human MCL-1ΔNΔC (Stewart et al., 2010) was expressed in transformed BL21(DE3) *E. coli*. Bacteria were grown at 37°C to an O.D. of 0.8, induced with 0.5 mM IPTG, pellets resuspended in lysis buffer (PBS with 1% [v/v] Triton X-100, complete protease inhibitor

tablet) and lysed by microfluidization. Lysates were cleared by centrifugation at 20,000 rpm for 45 min and subjected to glutathione Sepharose (GE Healthcare, Cat# 17-5132-01) affinity chromatography. For GST-tagged MCL-1ΔNΔC, the protein was eluted from the resin using 10 mM reduced glutathione (Sigma-Aldrich, Cat# G4251), whereas the tagless construct was generated by overnight cleavage with thrombin (GE Healthcare, Cat# 27-0846-01) in PBS. Recombinant MCL-1ΔNΔC was concentrated and subjected to size exclusion chromatography (GE Healthcare Life Sciences Superdex 75 10/300 GL) at 4°C using a 150 mM NaCl, 50 mM Tris, pH 7.4 buffer. Protein identification and purity was confirmed by intact mass spectrometry, SDS-PAGE, and either Coomassie staining or GST western analysis (GE Healthcare Life Sciences, Cat# 27-4577-01, RRID: AB_771432; 1:1000 in 3% [w/v] BSA).

^{19}F NMR Spectroscopy—Fluorinated SAHB (25 μM) and VLCAD (0–125 μM) were mixed in VLCAD FPLC buffer containing 10% (v/v) D_2O to a final volume of 500 μL. Samples were run on a Bruker Avance-III NMR spectrometer operating at 500 MHz using a room temperature fluorine inner-coil probe, and a pulse sequence that allows for direct observation of ^{19}F resonances in the presence of ^{1}H decoupling. Fluorine resonances were typically in the −60 to −65 ppm range. Quantification of binding was determined by measuring the peak width at half height ($\nu_{1/2}$) of the peptide ^{19}F signal. For the corresponding MCL-1ΔNΔC binding analyses, fluorinated SAHB (25 μM) and MCL-1ΔNΔC (0–45 μM) were used in the above-described method. As MCL-1ΔNΔC interaction induced a chemical shift of the ^{19}F peptide signal, binding was quantified by measuring the relative heights of the unbound and bound peptide peaks.

Biolayer Interferometry—Binding analysis by biolayer interferometry (BLI) was performed using an Octet Red384 System (ForteBio Inc.). Super streptavidin (SSA) sensors (Forte Bio, Cat# 18-5057) were pre-soaked in VLCAD FPLC buffer for at least 10 min prior to use, loaded with 5 μg/mL biotin-PEG-MCL-1 SAHBs for 400 sec, quenched with 0.1 mg/mL biocytin (Sigma-Aldrich, Cat# B4261) for 120 sec, and washed with VLCAD FPLC buffer for 120 sec. The sensors were then transferred into serial dilutions (starting at 30 μM) of VLCAD for 1800 sec. To measure binding to MCL-1ΔNΔC, SSA sensors were pre-soaked in MCL-1 FPLC buffer for at least 10 min prior to use, loaded with 5 μg/mL biotin-PEG-MCL-1 SAHBs for 400 sec, quenched with 0.1 mg/mL biocytin for 120 sec, and washed with kinetics buffer (Forte Bio, Cat# 18-1092) for 120 sec. The sensors were then transferred into serial dilutions (starting at 20 μM) of MCL-1ΔNΔC for 600 sec. Negative control runs were performed in parallel using sensors lacking biotin-PEG peptide and used as a reference for calculating the BLI baseline.

Affinity Labeling and Binding Site Analysis—Recombinant VLCAD protein (10 μM) and biotinylated pSAHB (40 μM) were mixed in 3 mL of VLCAD FPLC buffer, incubated at 4°C overnight, and irradiated (365 nm, Spectroline Handheld UV Lamp Model En280L, Spectronics) for 2 hours on ice (Braun et al., 2010). Unreacted peptide was removed by overnight dialysis at 4°C using 10 kDa molecular-weight cutoff Slide-A-Lyzer™ dialysis cassettes into VLCAD FPLC buffer. Biotinylated species were captured by incubating the reaction mixture with high capacity streptavidin agarose beads for 2 hours rotating at 4°C.

On-bead trypsin digestion was performed by incubating the beads at 60°C for 30 min in 100 μL of 50 mM ammonium bicarbonate, 5 mM DTT, and 0.1% (w/v) Rapigest (Waters, Cat# 186001861), followed by the addition of trypsin (0.1 μg) for overnight treatment at 37°C. To remove uncrosslinked VLCAD peptides, the beads were then washed at room temperature three times each in 1% (v/v) SDS in PBS, 1 M NaCl in PBS, and 10% (v/v) ethanol in PBS. Biotinylated species were eluted by incubating the beads in a 50% acetonitrile/0.1% TFA solution for 2 min at 65°C. MCL-1 pSAHB $_{D3}$-crosslinked samples were captured on streptavidin beads, washed and eluted as above, and then subjected to in-solution digestion. Samples were then purified through C18 OMIX tips and analyzed using a Thermo Orbitrap Discovery XL mass spectrometer, as described above (Braun et al., 2010).

Molecular Docking—The stapled peptide sequence RKALUTLRRVGDGVXRNHXTAF, where X is a stapling residue and U is 4-benzoyl-L-phenylalanine, was built using Maestro (Schrödinger, LLC) as an idealized α-helix. The sequence was docked to the crystal structure of VLCAD (PDB: 3B96) using the HADDOCK 2.2 webserver default parameters (van Zundert et al., 2016). Based on the crosslinking results, residues S32, F38, T240, F242, R246, G250, V292, M294, and S445 were defined as active residues in the docking calculations, with passive residues defined automatically. All stapled peptide residues were treated as active. Top-scoring clusters were analyzed visually using Pymol (Schrödinger, LLC) for consistency with the experimentally-determined crosslinking data. Select clusters were then refined using molecular mechanics minimization in the Schrodinger software suite (Version 2016-2). The H bond network of the protein was optimized and the protein/peptide complex was minimized using the OPLS3 force field (Harder et al., 2016).

Hydrogen-Deuterium Exchange Mass Spectrometry—Hydrogen-deuterium exchange mass spectrometry (HXMS) experiments were performed as described (Barclay et al., 2015). Briefly, deuterium labeling was initiated with an 18-fold dilution into D_2O buffer (50 mM Tris, 150 mM NaCl, pD 7.6) of a pre-equilibrated (5 min, room temperature) aliquot of VLCADΔEx3 or VLCADΔEx3 combined with 10-fold molar excess of MCL-1 SAHB$_D$ V220A. After 10 seconds of labeling, the labeling reaction was quenched with the addition of an equal volume of quenching buffer (0.8 M guanidinium chloride, 0.8% [v/v] formic acid). Samples were then injected and inline digested using a self-packed pepsin column (2.1 mm × 50 mm, pepsin immobilized on POROS-20AL beads) (Wang et al., 2002; Wu et al., 2006). The peptides were trapped and desalted on a VanGuard Pre-Column trap (2.1 × 5 mm, ACQUITY UPLC BEH C18, 1.7 μm) for 3 min, eluted from the trap using a 5–35% gradient of acetonitrile over 6 min at a flow rate of 65 μL/min, and then separated using an ACQUITY UPLC HSS T3, 1.8 μm, 1.0 × 50 mm column on a Waters nanoACQUITY LC. The Waters Synapt G2Si mass spectrometer was operated in ion mobility mode and data analyzed as described (Barclay et al., 2015). Peptides from an unlabeled protein were identified using ProteinLynx Global Server (PLGS) searches of a protein database including analyte protein. The relative deuterium levels of identified peptides common to both evaluated conditions are shown. The error of determining the average deuterium incorporation for each peptide was at or below ± 0.25 Da. Relative deuterium levels for each peptide were calculated by subtracting the average mass of the undeuterated control sample from that of the deuterium-labeled sample. All mass spectra

were processed using DynamX 3.0 (Waters Corporation). Deuterium levels were not corrected for back exchange and thus reported as relative (Wales and Engen, 2006). Data is representative of two biological replicates.

Acylcarnitine Analysis—MEFs were plated in Minimum Essential Media (MEM; Invitrogen) containing 200 μM palmitic acid (Sigma-Aldrich, Cat# P0500), 50 μM fatty-acid-free bovine serum albumin (BSA) (Sigma-Aldrich, Cat# A8806) and 400 μM L-carnitine (Sigma-Aldrich, Cat# C0283) for 96 hours. Palmitic acid-containing media (Shen et al., 2000) was generated as follows: (1) a stock solution of palmitic acid was prepared in ethanol, pipetted into a bottle, and dried under nitrogen; (2) BSA was dissolved in MEM by brief sonication and gentle shaking at 37°C for 1 hour; (3) the media was then added to the dry palmitic acid, sonicated briefly, and allowed to shake gently overnight at 37°C, followed by addition of L-carnitine, FBS, and glutamine. For tamoxifen-induced deletion of *Mcl-1*, cells were treated with tamoxifen or vehicle prior to the above incubation in palmitic acid-containing media. Cells were then trypsinized, washed with cold PBS, flash frozen in liquid nitrogen, and stored at −80°C. Liver tissue was isolated from *Mcl-1*$^{fl/fl}$ mice two weeks after co-infection by tail vein with scAAV-LP1-Cre and scAAV-LP1-GFP or co-infection with scAAV-LP1-Cre and scAAV-LP1-MCL-1 vectors, and flash frozen in liquid nitrogen and stored at −80°C. Frozen cell pellets and liver tissue were thawed in 1 mL of a 3:1 acetonitrile:methanol solution containing 0.1 μM ^{13}C-palmitoyl-L-carnitine (Sigma-Aldrich, Cat# 644323) as an internal standard. Once thawed, cells were thoroughly re-suspended by two rounds of vortexing and sonication for 30 sec each, whereas liver tissue was homogenized thoroughly with an IKA T10 Basic homogenizer. Debris was pelleted at 12,000×g for 10 min, after which the supernatant was transferred to a clean tube and dried under nitrogen at 45°C. Acylcarnitine species were butylated by the addition of 100 μL acetyl chloride (Sigma-Aldrich) and 400 μL 1-butanol (Sigma-Aldrich) for 15 min at 60°C (Chegary et al., 2008). Samples were then dried again, resuspended in 100% acetonitrile, and run on a Thermo Ultimate 3000 uHPLC coupled to a Q-Exactive Plus mass spectrometer (Chegary et al., 2008). Data were analyzed using the Xcalibur Qual Browser (Thermo v3.0.63).

Fatty Acid Oxidation Assays—MEFs (10^5/well) were plated in six-well plates, allowed to adhere overnight, and then pre-incubated in either serum-containing or serum-free medium for 2 hours. Cells were then changed to medium containing 1μCi [9,10(n)-^{3}H]palmitic acid (Perkin-Elmer, Cat# NET043001MC) or 1.8 μCi n-[5,6-^{3}H]hexanoic acid (American Radiolabeled Chemicals Inc., Cat# ART 1754-250) and 1 mM carnitine for 2 hours, maintaining serum-containing or serum-free conditions. The medium was collected and eluted in columns packed with DOWEX 1X2-400 ion exchange resin (Sigma-Aldrich, Cat# 217395) to analyze the released ^3H_2O. Counts per min (CPM) were normalized to protein content in cell lysates. For cells treated with S63845 (Active Biochem, Cat# A-6044), the compound was added to the cells with [9,10(n)-^{3}H]palmitic acid for two hours at a final sub-cytotoxic concentration of 1 μM. For tamoxifen-induced deletion of *Mcl-1*, cells were treated with tamoxifen or vehicle for 48 hours and allowed to recover for an additional 48 hours prior to conducting the experiment.

Dynamic Assessment of MCL-1 Protein Levels—MEFs (10^5/well) were plated in serum-containing DMEM in 2 wells of a six-well plate per time point and allowed to adhere. Media was then replaced with serum-free DMEM and cells harvested and lysed at the indicated time points. Cell lysates were subjected to electrophoresis and western blotting for MCL-1 and actin (Sigma-Aldrich, Cat# A1978, RRID: AB_476692; 1:1500 in 3% [w/v] BSA).

VLCAD Enzymatic Analysis—VLCAD enzymatic activity was measured as previously described (Doulias et al., 2013; Lehman et al., 1990). Ferrocenium hexafluorophosphate (Sigma-Aldrich, Cat# 388297) was dissolved in 10 mM HCl to a concentration of 1 mM, further diluted to a final concentration of 150 μM in assay buffer (100 mM potassium phosphate, pH 7.2, 0.1 mM EDTA) and added to 300 μM palmitoyl-CoA. The reaction was initiated by addition of purified recombinant VLCAD protein (final concentration of 0.72 μM) that had been incubated overnight at 4°C with either vehicle (1.5% [v/v] DMSO) or MCL-1 SAHB (final concentration of 72 μM). Decrease in ferrocenium absorbance as a function of time at 300 nm was recorded and the initial velocity (V_0) calculated in units of U/mg using the molar absorptivity of ferrocenium ($\varepsilon = 4.3\ mM^{-1}cm^{-1}$ at 300 nm).

Gene Set Enrichment Analyses—Gene expression matrices of AML datasets were retrieved by Qlucore v3.3 with the GEO accession numbers GEO: GSE14468 (Wouters et al., 2009) and GSE1159 (Valk et al., 2004). Patient samples were dichotomized into two subgroups based on the percentile of *Mcl-1* expression (0–50% vs 50–100%), and the association between *Mcl-1* expression and FAO pathways analyzed using GSEA v3.0 with default parameters (Mootha et al., 2003; Subramanian et al., 2005).

QUANTIFICATION AND STATISTICAL ANALYSIS

Data are expressed as mean ± S.D. unless otherwise noted. Exact numbers of biological and technical replicates for each experiment are reported in the Figure Legends. p values less than 0.05 were considered statistically significant by unpaired, two-tailed Student's t test. For all data, *, $p \leq 0.05$; **, $p \leq 0.01$; ***, $p \leq 0.0001$. Data were analyzed using Prism Software 7.0 (GraphPad).

DATA AND SOFTWARE AVAILABILITY

N/A

Supplementary Material

Refer to Web version on PubMed Central for supplementary material.

Acknowledgments

We thank E. Smith for graphics support; S. Trauger, W. Massefski, K. Arnett, and M. Bathina for expert technical assistance with mass spectrometry, NMR spectroscopy, biolayer interferometry, and animal husbandry, respectively; T. Oo for peptide synthesis; and A. Moreno, N. Danial, A. Saghatelian, C. Braun, S. Gygi, H. Herce, K. Szarama, Y. Zhang, and J. Schuetz for helpful discussions. This work was supported by NIH grant 1R35CA197583 and a Leukemia and Lymphoma Scholar Award #1299-15 to L.D.W., a National Science Foundation Predoctoral Award to S.E., NIH grant 1R50CA211399 to G.H.B., NIH grant T32GM007753 to A.M.M. and J.L., Doctoral Foreign

Studies Award DFS-134963 from the Canadian Institutes of Health Research to R.M., NIH grant 5R01HL123543 to J.T.O., NIH grants 5R01CA166429 and 1R01CA217092 to U.S, and NIH grant 5R01DK103295 to M.C.H.

References

Aouacheria A, Combet C, Tompa P, Hardwick JM. Redefining the BH3 Death Domain as a 'Short Linear Motif'. Trends Biochem Sci. 2015; 40:736–748. [PubMed: 26541461]

Baeza J, Smallegan MJ, Denu JM. Mechanisms and Dynamics of Protein Acetylation in Mitochondria. Trends Biochem Sci. 2016; 41:231–244. [PubMed: 26822488]

Barclay LA, Wales TE, Garner TP, Wachter F, Lee S, Guerra RM, Stewart ML, Braun CR, Bird GH, Gavathiotis E, et al. Inhibition of Pro-apoptotic BAX by a noncanonical interaction mechanism. Mol Cell. 2015; 57:873–886. [PubMed: 25684204]

Beroukhim R, Mermel CH, Porter D, Wei G, Raychaudhuri S, Donovan J, Barretina J, Boehm JS, Dobson J, Urashima M, et al. The landscape of somatic copy-number alteration across human cancers. Nature. 2010; 463:899–905. [PubMed: 20164920]

Bird GH, Crannell WC, Walensky LD. Chemical synthesis of hydrocarbon-stapled peptides for protein interaction research and therapeutic targeting. Curr Protoc Chem Biol. 2011; 3:99–117. [PubMed: 23801563]

Braun CR, Mintseris J, Gavathiotis E, Bird GH, Gygi SP, Walensky LD. Photoreactive stapled BH3 peptides to dissect the BCL-2 family interactome. Chem Biol. 2010; 17:1325–1333. [PubMed: 21168768]

Caro P, Kishan AU, Norberg E, Stanley IA, Chapuy B, Ficarro SB, Polak K, Tondera D, Gounarides J, Yin H, et al. Metabolic signatures uncover distinct targets in molecular subsets of diffuse large B cell lymphoma. Cancer Cell. 2012; 22:547–560. [PubMed: 23079663]

Certo M, Del Gaizo Moore V, Nishino M, Wei G, Korsmeyer S, Armstrong SA, Letai A. Mitochondria primed by death signals determine cellular addiction to antiapoptotic BCL-2 family members. Cancer Cell. 2006; 9:351–365. [PubMed: 16697956]

Chegary M, Te Brinke H, Doolaard M, Ijlst L, Wijburg FA, Wanders RJ, Houten SM. Characterization of L-aminocarnitine, an inhibitor of fatty acid oxidation. Mol Genet Metab. 2008; 93:403–410. [PubMed: 18077198]

Cheng EH, Wei MC, Weiler S, Flavell RA, Mak TW, Lindsten T, Korsmeyer SJ. BCL-2, BCL-X(L) sequester BH3 domain-only molecules preventing BAX- and BAK-mediated mitochondrial apoptosis. Mol Cell. 2001; 8:705–711. [PubMed: 11583631]

Danial NN, Gramm CF, Scorrano L, Zhang CY, Krauss S, Ranger AM, Datta SR, Greenberg ME, Licklider LJ, Lowell BB, et al. BAD and glucokinase reside in a mitochondrial complex that integrates glycolysis and apoptosis. Nature. 2003; 424:952–956. [PubMed: 12931191]

Danial NN, Korsmeyer SJ. Cell death: critical control points. Cell. 2004; 116:205–219. [PubMed: 14744432]

Danial NN, Walensky LD, Zhang CY, Choi CS, Fisher JK, Molina AJ, Datta SR, Pitter KL, Bird GH, Wikstrom JD, et al. Dual role of proapoptotic BAD in insulin secretion and beta cell survival. Nat Med. 2008; 14:144–153. [PubMed: 18223655]

DeBerardinis RJ, Mancuso A, Daikhin E, Nissim I, Yudkoff M, Wehrli S, Thompson CB. Beyond aerobic glycolysis: transformed cells can engage in glutamine metabolism that exceeds the requirement for protein and nucleotide synthesis. Proc Natl Acad Sci U S A. 2007; 104:19345–19350. [PubMed: 18032601]

Diz AP, Carvajal-Rodriguez A, Skibinski DO. Multiple hypothesis testing in proteomics: a strategy for experimental work. Mol Cell Proteomics. 2011; 10:M110004374.

Doulias PT, Tenopoulou M, Greene JL, Raju K, Ischiropoulos H. Nitric oxide regulates mitochondrial fatty acid metabolism through reversible protein S-nitrosylation. Sci Signal. 2013; 6:rs1. [PubMed: 23281369]

Engen JR. Analysis of protein conformation and dynamics by hydrogen/deuterium exchange MS. Anal Chem. 2009; 81:7870–7875. [PubMed: 19788312]

German NJ, Yoon H, Yusuf RZ, Murphy JP, Finley LW, Laurent G, Haas W, Satterstrom FK, Guarnerio J, Zaganjor E, et al. PHD3 Loss in Cancer Enables Metabolic Reliance on Fatty Acid Oxidation via Deactivation of ACC2. Mol Cell. 2016; 63:1006–1020. [PubMed: 27635760]

Goetzman ES, Wang Y, He M, Mohsen AW, Ninness BK, Vockley J. Expression and characterization of mutations in human very long-chain acyl-CoA dehydrogenase using a prokaryotic system. Mol Genet Metab. 2007; 91:138–147. [PubMed: 17374501]

Gokce E, Shuford CM, Franck WL, Dean RA, Muddiman DC. Evaluation of normalization methods on GeLC-MS/MS label-free spectral counting data to correct for variation during proteomic workflows. J Am Soc Mass Spectrom. 2011; 22:2199–2208. [PubMed: 21952779]

Harder E, Damm W, Maple J, Wu C, Reboul M, Xiang JY, Wang L, Lupyan D, Dahlgren MK, Knight JL, et al. OPLS3: A Force Field Providing Broad Coverage of Drug-like Small Molecules and Proteins. J Chem Theory Comput. 2016; 12:281–296. [PubMed: 26584231]

Kamer I, Sarig R, Zaltsman Y, Niv H, Oberkovitz G, Regev L, Haimovich G, Lerenthal Y, Marcellus RC, Gross A. Proapoptotic BID is an ATM effector in the DNA-damage response. Cell. 2005; 122:593–603. [PubMed: 16122426]

Karbowski M, Norris KL, Cleland MM, Jeong SY, Youle RJ. Role of Bax and Bak in mitochondrial morphogenesis. Nature. 2006; 443:658–662. [PubMed: 17035996]

Kotschy A, Szlavik Z, Murray J, Davidson J, Maragno AL, Le Toumelin-Braizat G, Chanrion M, Kelly GL, Gong JN, Moujalled DM, et al. The MCL1 inhibitor S63845 is tolerable and effective in diverse cancer models. Nature. 2016; 538:477–482. [PubMed: 27760111]

Lee KM, Giltnane JM, Balko JM, Schwarz LJ, Guerrero-Zotano AL, Hutchinson KE, Nixon MJ, Estrada MV, Sanchez V, Sanders ME, et al. MYC and MCL1 Cooperatively Promote Chemotherapy-Resistant Breast Cancer Stem Cells via Regulation of Mitochondrial Oxidative Phosphorylation. Cell Metab. 2017; 26:633–647. e637. [PubMed: 28978427]

Lehman TC, Hale DE, Bhala A, Thorpe C. An acyl-coenzyme A dehydrogenase assay utilizing the ferricenium ion. Anal Biochem. 1990; 186:280–284. [PubMed: 2363500]

McAndrew RP, Wang Y, Mohsen AW, He M, Vockley J, Kim JJ. Structural basis for substrate fatty acyl chain specificity: crystal structure of human very-long-chain acyl-CoA dehydrogenase. J Biol Chem. 2008; 283:9435–9443. [PubMed: 18227065]

Mellacheruvu D, Wright Z, Couzens AL, Lambert JP, St-Denis NA, Li T, Miteva YV, Hauri S, Sardiu ME, Low TY, et al. The CRAPome: a contaminant repository for affinity purification-mass spectrometry data. Nat Methods. 2013; 10:730–736. [PubMed: 23921808]

Mootha VK, Lindgren CM, Eriksson KF, Subramanian A, Sihag S, Lehar J, Puigserver P, Carlsson E, Ridderstrale M, Laurila E, et al. PGC-1alpha-responsive genes involved in oxidative phosphorylation are coordinately downregulated in human diabetes. Nat Genet. 2003; 34:267–273. [PubMed: 12808457]

Nathwani AC, Cochrane M, McIntosh J, Ng CY, Zhou J, Gray JT, Davidoff AM. Enhancing transduction of the liver by adeno-associated viral vectors. Gene Ther. 2009; 16:60–69. [PubMed: 18701909]

Opferman JT, Iwasaki H, Ong CC, Suh H, Mizuno S, Akashi K, Korsmeyer SJ. Obligate role of anti-apoptotic MCL-1 in the survival of hematopoietic stem cells. Science. 2005; 307:1101–1104. [PubMed: 15718471]

Opferman JT, Letai A, Beard C, Sorcinelli MD, Ong CC, Korsmeyer SJ. Development and maintenance of B and T lymphocytes requires antiapoptotic MCL-1. Nature. 2003; 426:671–676. [PubMed: 14668867]

Pascual G, Avgustinova A, Mejetta S, Martin M, Castellanos A, Attolini CS, Berenguer A, Prats N, Toll A, Hueto JA, et al. Targeting metastasis-initiating cells through the fatty acid receptor CD36. Nature. 2017; 541:41–45. [PubMed: 27974793]

Perciavalle RM, Stewart DP, Koss B, Lynch J, Milasta S, Bathina M, Temirov J, Cleland MM, Pelletier S, Schuetz JD, et al. Anti-apoptotic MCL-1 localizes to the mitochondrial matrix and couples mitochondrial fusion to respiration. Nat Cell Biol. 2012; 14:575–583. [PubMed: 22544066]

Rebsamen M, Pochini L, Stasyk T, de Araujo ME, Galluccio M, Kandasamy RK, Snijder B, Fauster A, Rudashevskaya EL, Bruckner M, et al. SLC38A9 is a component of the lysosomal amino acid sensing machinery that controls mTORC1. Nature. 2015; 519:477–481. [PubMed: 25561175]

Rinkenberger JL, Horning S, Klocke B, Roth K, Korsmeyer SJ. Mcl-1 deficiency results in peri-implantation embryonic lethality. Genes Dev. 2000; 14:23–27. [PubMed: 10640272]

Samudio I, Harmancey R, Fiegl M, Kantarjian H, Konopleva M, Korchin B, Kaluarachchi K, Bornmann W, Duvvuri S, Taegtmeyer H, et al. Pharmacologic inhibition of fatty acid oxidation sensitizes human leukemia cells to apoptosis induction. J Clin Invest. 2010; 120:142–156. [PubMed: 20038799]

Sattler M, Liang H, Nettesheim D, Meadows RP, Harlan JE, Eberstadt M, Yoon HS, Shuker SB, Chang BS, Minn AJ, et al. Structure of Bcl-xL-Bak peptide complex: recognition between regulators of apoptosis. Science. 1997; 275:983–986. [PubMed: 9020082]

Shen JJ, Matern D, Millington DS, Hillman S, Feezor MD, Bennett MJ, Qumsiyeh M, Kahler SG, Chen YT, Van Hove JL. Acylcarnitines in fibroblasts of patients with long-chain 3-hydroxyacyl-CoA dehydrogenase deficiency and other fatty acid oxidation disorders. J Inherit Metab Dis. 2000; 23:27–44. [PubMed: 10682306]

Smith B, Schafer XL, Ambeskovic A, Spencer CM, Land H, Munger J. Addiction to Coupling of the Warburg Effect with Glutamine Catabolism in Cancer Cells. Cell Rep. 2016; 17:821–836. [PubMed: 27732857]

Souers AJ, Leverson JD, Boghaert ER, Ackler SL, Catron ND, Chen J, Dayton BD, Ding H, Enschede SH, Fairbrother WJ, et al. ABT-199, a potent and selective BCL-2 inhibitor, achieves antitumor activity while sparing platelets. Nat Med. 2013; 19:202–208. [PubMed: 23291630]

Stewart ML, Fire E, Keating AE, Walensky LD. The MCL-1 BH3 helix is an exclusive MCL-1 inhibitor and apoptosis sensitizer. Nat Chem Biol. 2010; 6:595–601. [PubMed: 20562877]

Strauss AW, Powell CK, Hale DE, Anderson MM, Ahuja A, Brackett JC, Sims HF. Molecular basis of human mitochondrial very-long-chain acyl-CoA dehydrogenase deficiency causing cardiomyopathy and sudden death in childhood. Proc Natl Acad Sci U S A. 1995; 92:10496–10500. [PubMed: 7479827]

Subramanian A, Tamayo P, Mootha VK, Mukherjee S, Ebert BL, Gillette MA, Paulovich A, Pomeroy SL, Golub TR, Lander ES, et al. Gene set enrichment analysis: a knowledge-based approach for interpreting genome-wide expression profiles. Proc Natl Acad Sci U S A. 2005; 102:15545–15550. [PubMed: 16199517]

Tsujimoto Y, Finger LR, Yunis J, Nowell PC, Croce CM. Cloning of the chromosome breakpoint of neoplastic B cells with the t(14;18) chromosome translocation. Science. 1984; 226:1097–1099. [PubMed: 6093263]

Valk PJ, Verhaak RG, Beijen MA, Erpelinck CA, Barjesteh van Waalwijk van Doorn-Khosrovani S, Boer JM, Beverloo HB, Moorhouse MJ, van der Spek PJ, Lowenberg B, et al. Prognostically useful gene-expression profiles in acute myeloid leukemia. N Engl J Med. 2004; 350:1617–1628. [PubMed: 15084694]

van Zundert GC, Rodrigues JP, Trellet M, Schmitz C, Kastritis PL, Karaca E, Melquiond AS, van Dijk M, de Vries SJ, Bonvin AM. The HADDOCK2.2 Web Server: User-Friendly Integrative Modeling of Biomolecular Complexes. J Mol Biol. 2016; 428:720–725. [PubMed: 26410586]

Wajner M, Amaral AU. Mitochondrial dysfunction in fatty acid oxidation disorders: insights from human and animal studies. Biosci Rep. 2015; 36:e00281. [PubMed: 26589966]

Walensky LD, Bird GH. Hydrocarbon-stapled peptides: principles, practice, and progress. J Med Chem. 2014; 57:6275–6288. [PubMed: 24601557]

Walensky LD, Gavathiotis E. BAX unleashed: the biochemical transformation of an inactive cytosolic monomer into a toxic mitochondrial pore. Trends Biochem Sci. 2011; 36:642–652. [PubMed: 21978892]

Wales TE, Engen JR. Hydrogen exchange mass spectrometry for the analysis of protein dynamics. Mass Spectrom Rev. 2006; 25:158–170. [PubMed: 16208684]

Wang L, Pan H, Smith DL. Hydrogen exchange-mass spectrometry: optimization of digestion conditions. Mol Cell Proteomics. 2002; 1:132–138. [PubMed: 12096131]

Wang M, Herrmann CJ, Simonovic M, Szklarczyk D, von Mering C. Version 4.0 of PaxDb: Protein abundance data, integrated across model organisms, tissues, and cell-lines. Proteomics. 2015; 15:3163–3168. [PubMed: 25656970]

Wang X, Bathina M, Lynch J, Koss B, Calabrese C, Frase S, Schuetz JD, Rehg JE, Opferman JT. Deletion of MCL-1 causes lethal cardiac failure and mitochondrial dysfunction. Genes Dev. 2013; 27:1351–1364. [PubMed: 23788622]

Wouters BJ, Lowenberg B, Erpelinck-Verschueren CA, van Putten WL, Valk PJ, Delwel R. Double CEBPA mutations, but not single CEBPA mutations, define a subgroup of acute myeloid leukemia with a distinctive gene expression profile that is uniquely associated with a favorable outcome. Blood. 2009; 113:3088–3091. [PubMed: 19171880]

Wu Y, Kaveti S, Engen JR. Extensive deuterium back-exchange in certain immobilized pepsin columns used for H/D exchange mass spectrometry. Anal Chem. 2006; 78:1719–1723. [PubMed: 16503628]

Xiong D, He H, James J, Tokunaga C, Powers C, Huang Y, Osinska H, Towbin JA, Purevjav E, Balschi JA, et al. Cardiac-specific VLCAD deficiency induces dilated cardiomyopathy and cold intolerance. Am J Physiol Heart Circ Physiol. 2014; 306:H326–338. [PubMed: 24285112]

Youle RJ, Strasser A. The BCL-2 protein family: opposing activities that mediate cell death. Nat Rev Mol Cell Biol. 2008; 9:47–59. [PubMed: 18097445]

Zinkel SS, Hurov KE, Ong C, Abtahi FM, Gross A, Korsmeyer SJ. A role for proapoptotic BID in the DNA-damage response. Cell. 2005; 122:579–591. [PubMed: 16122425]

HIGHLIGHTS

- The MCL-1 BH3 helix directly interacts with and modulates VLCAD
- *Mcl-1* deletion deregulates long-chain fatty acid β-oxidation
- The mitochondrial matrix form of MCL-1 has a separable function in lipid metabolism
- MCL-1 exerts dual control over mitochondrial apoptosis and fatty acid metabolism

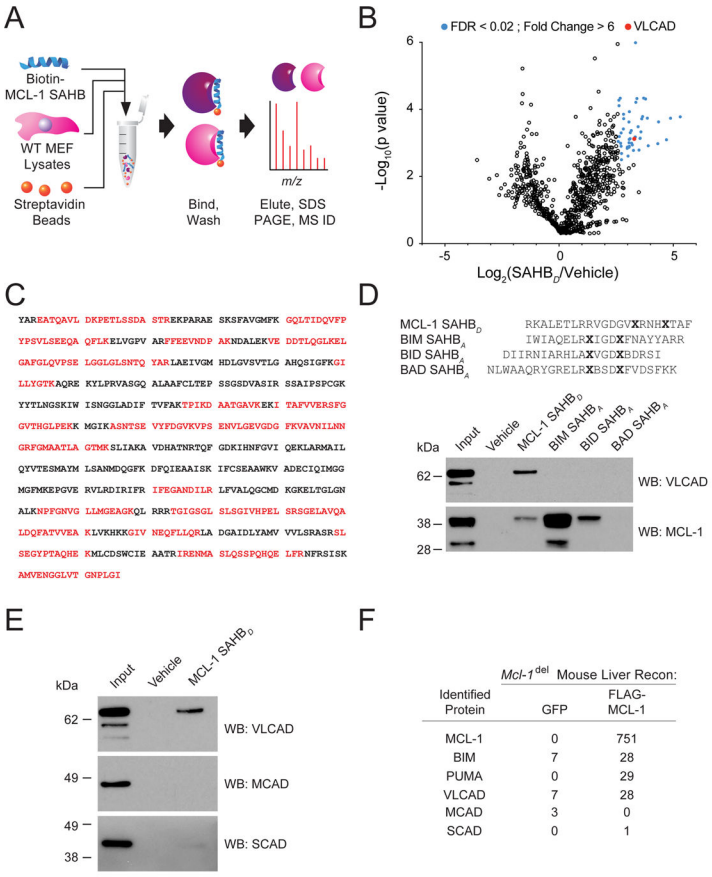

Figure 1. Identification of VLCAD as an MCL-1-Interacting Protein

(A) Proteomics workflow for streptavidin capture and identification of MEF lysate proteins that bound to a biotinylated and stapled MCL-1 BH3 helix.

(B) Volcano plot demonstrating the distribution of identified proteins and high-confidence MCL-1 SAHB$_D$ interactors (blue), including VLCAD (red). Pull-down experiments and mass spectrometry analyses were performed in biological triplicate.

(C) VLCAD was identified as a high-stringency hit with 49% sequence coverage (red) by mass spectrometry.

(D) Interaction profiles of MCL-1, BIM, BID, and BAD BH3 stapled peptide helices with native MCL-1 and VLCAD, as demonstrated by streptavidin pull-down from MEF lysates, and MCL-1 and VLCAD western analyses.

(E) Selective interaction of MCL-1 SAHB$_D$ with native VLCAD but not other members of the acyl-CoA dehydrogenase family, such as MCAD and SCAD, as assessed by streptavidin pull-down from MEF lysates, and VLCAD, MCAD, and SCAD western analyses.

(F) Similar enrichment for native, full-length BIM, PUMA, and VLCAD proteins, but not MCAD or SCAD, in FLAG-MCL-1 immunoprecipitations from mouse liver mitochondria, isolated from *Mcl-1*$^{fl/fl}$ mice co-infected with scAAV-LP1-Cre and either scAAV-LP1-FLAG-MCL-1 or scAAV-LP1-GFP, and analyzed by mass spectrometry. Each immunoprecipitation represents the pooled mitochondria from 3 independent mice, and the mass spectrometry analysis was performed in duplicate.

See also Figures S1–S2 and Tables S1–S2.

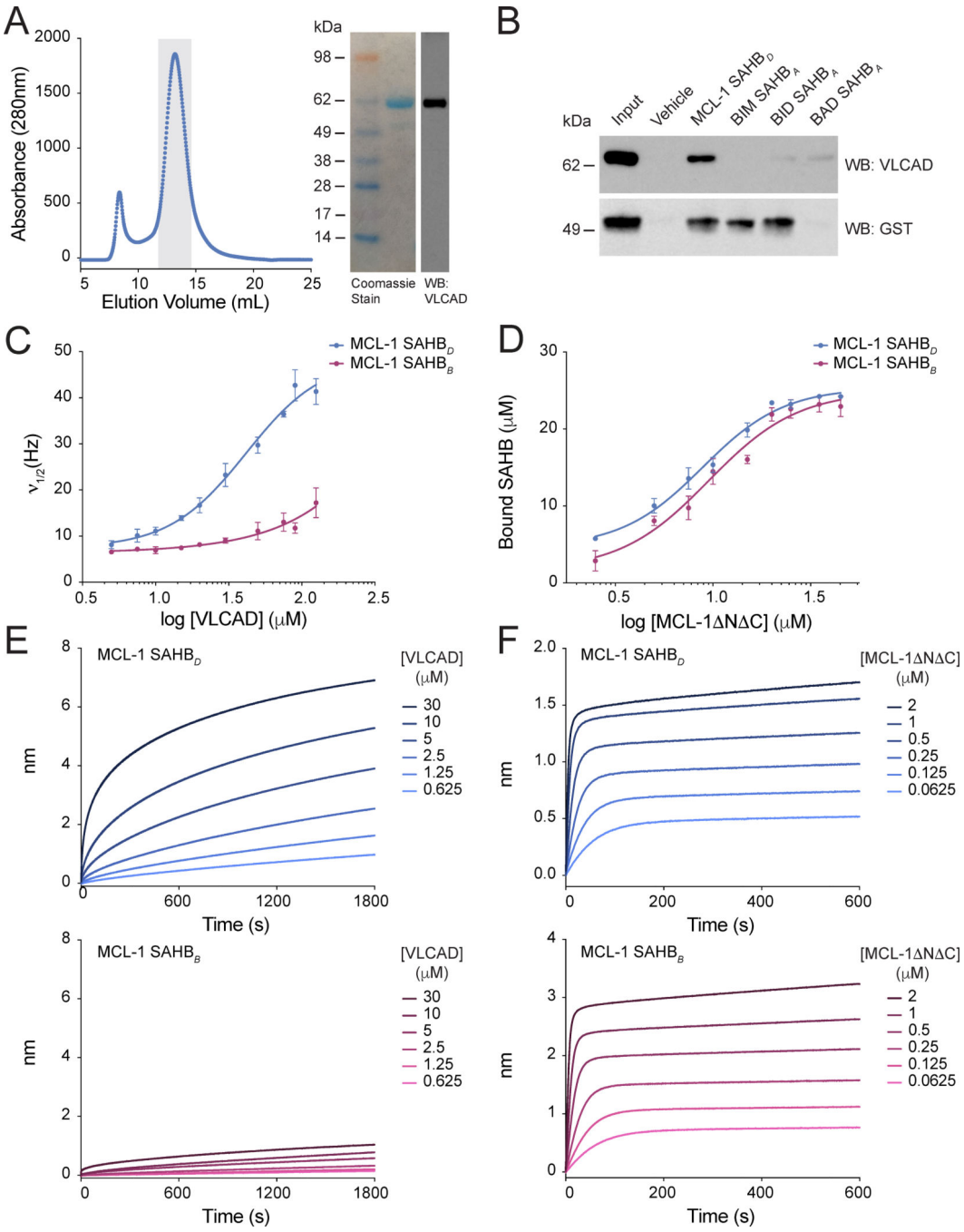

Figure 2. MCL-1 SAHB$_D$ Directly and Selectively Binds to VLCAD

(A) Expression and purification of recombinant VLCAD, as demonstrated by size exclusion chromatography profile, Coomassie staining, and VLCAD western analysis. The collected peak corresponding to the obligate dimer is shaded in gray.

(B) Interaction profiles of MCL-1, BIM, BID, and BAD BH3 stapled peptide helices with recombinant VLCAD and GST-MCL-1ΔNΔC, as demonstrated by streptavidin pull-down, and VLCAD and GST western analyses.

(C–D) ^{19}F NMR binding analyses demonstrated selective interaction of recombinant VLCAD with MCL-1 SAHB$_D$ (blue), but not MCL-1 SAHB$_B$ (purple) (C), whereas MCL-1ΔNΔC engaged with both SAHB constructs similarly (D). Data are mean ± S.D. for experiments performed in biological triplicate.

(E–F) Comparative binding of MCL-1 SAHB$_D$ (blue) and MCL-1 SAHB$_B$ (purple) to recombinant VLCAD (E) and MCL-1ΔNΔC (F), as measured by biolayer interferometry, corroborated the ^{19}F NMR findings. Representative traces are shown for BLI experiments performed in biological triplicate.

See also Figures S2–S3, and Table S1.

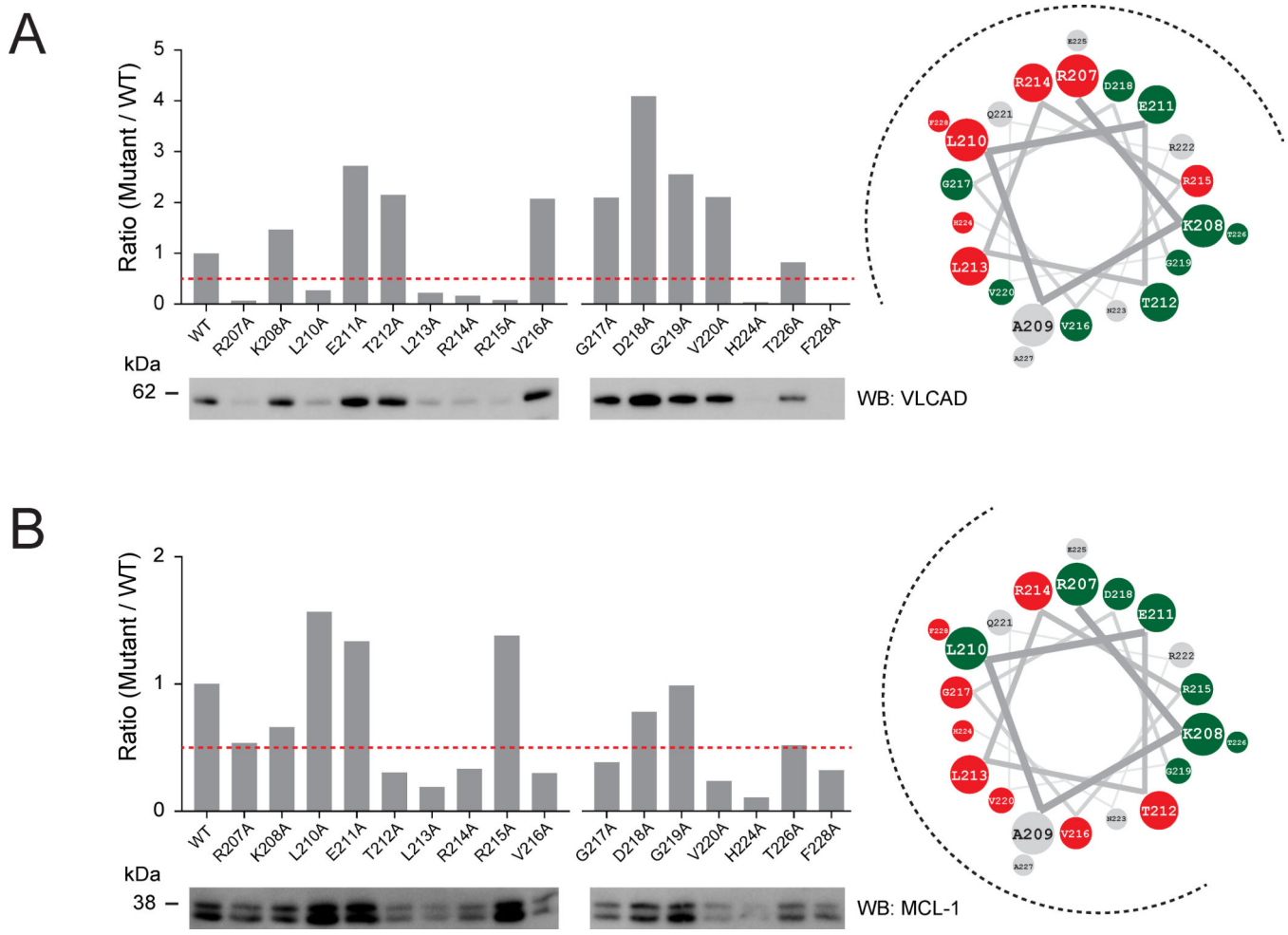

Figure 3. Sequence Determinants for MCL-1 SAHB$_D$ Interaction with VLCAD

(A–B) Differential influence of alanine mutagenesis on the interactions between Btn-MCL-1 SAHB$_D$ and native VLCAD (A) and MCL-1 (B), as assessed by western blotting of streptavidin pull-downs from MEF lysates and densitometric analysis. Alanine mutations that reduced the wild-type interaction by more than 50% (red dotted line) are colored red on the helical wheels, whereas those constructs demonstrating less of a negative influence, no effect, or a binding enhancement are colored green. Native alanines and residues not mutated are colored gray. The dotted semicircles highlight the distinctive MCL-1 BH3 binding interfaces for VLCAD versus MCL-1 engagement, as defined by the differential sensitivities to alanine mutagenesis. The pull-downs were performed twice with similar results.

See also Table S1.

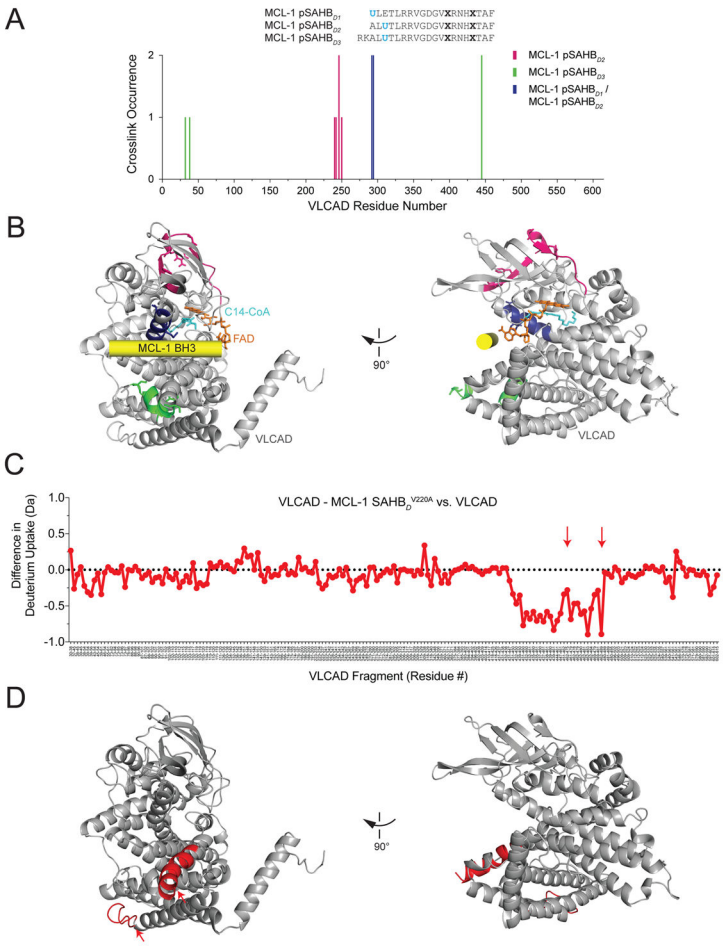

Figure 4. Localization of the MCL-1 BH3 Binding Site on VLCAD

(A) Photoaffinity labeling of VLCAD by biotinylated MCL-1 pSAHBs that incorporate a benzophenone-containing residue (U). The plot represents the frequency and location of Btn-pSAHB/VLCAD crosslinks, as determined by LC-MS/MS analysis of biotinylated, streptavidin-captured, and trypsinized VLCAD protein.

(B) Mapping of the pSAHB-crosslinked peptide fragments and specific residues (purple, green, and blue ribbons, and sticks, respectively) onto the VLCAD structure (PDB: 3B96) revealed their localization to a surface groove, where molecular docking calculations placed the MCL-1 BH3 helix (yellow cylinder). Intriguingly, fatty acid substrate (cyan) and the FAD co-factor (orange) lie adjacent to the putative helix-in-groove interaction.

(C) The addition of MCL-SAHB$_D$V220A to VLCAD (20 μM, 10:1 MCL-1 SAHB:VLCAD, 5 min incubation/10 sec deuteration) triggered a regiospecific decrease in deuterium incorporation compared to unliganded VLCAD, as measured by HXMS. The difference in deuterium uptake plot reflects the relative deuterium incorporation of MCL-1 SAHB/VLCAD minus the relative deuterium incorporation of VLCAD. Red arrows demarcate the boundary of the loop absent from the crystal structure of VLCAD (PDB: 3B96). Data are representative of two independent experiments.

(D) The region of MCL-1 SAHB-induced protection encompasses peptide fragments corresponding to amino acids 431–489, which are highlighted in red on the ribbon diagram

(PDB: 3B96) and map to the α-helical 2 region of VLCAD and the subjacent loop not found in the crystal structure (arrows).
See also Table S1.

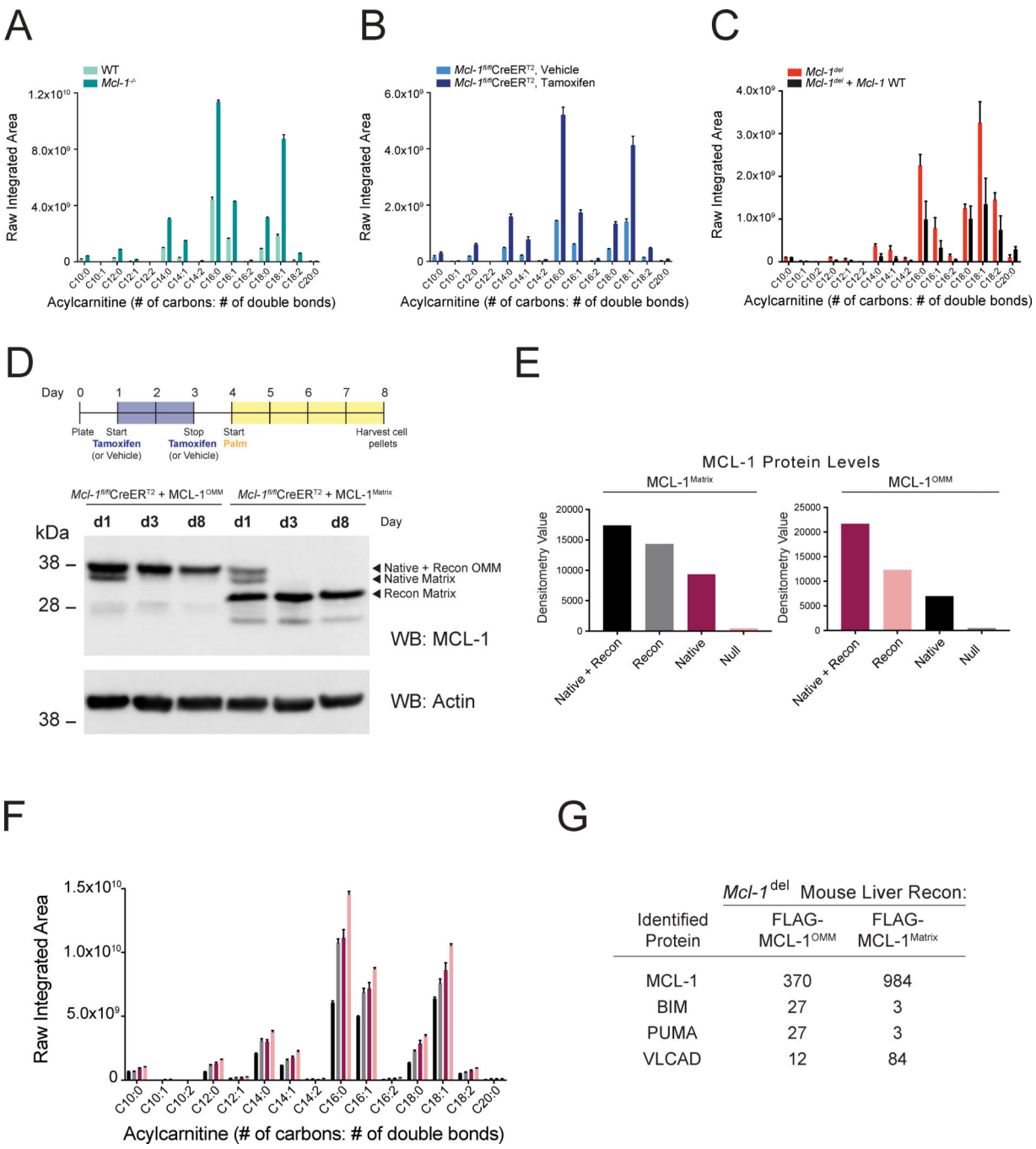

G

Identified Protein	Mcl-1 del Mouse Liver Recon: FLAG-MCL-1 OMM	FLAG-MCL-1 Matrix
MCL-1	370	984
BIM	27	3
PUMA	27	3
VLCAD	12	84

Figure 5. Elevated Long-Chain Fatty Acylcarnitine Levels upon *Mcl-1* Deletion

(A–B) Both chronic (*Mcl-1*$^{-/-}$) (A) and acute (*Mcl-1*$^{fl/fl}$CreER^{T2}, Tamoxifen) (B) deletion of *Mcl-1* led to a similar profile of elevated long-chain fatty acylcarnitines compared to the corresponding control MEFs (wild-type and *Mcl-1*$^{fl/fl}$CreER^{T2}, vehicle, respectively), as monitored by mass spectrometry of cellular lipid extracts. Error bars are mean ± S.D. for experiments performed in technical triplicate (A) and quadruplicate (B).

(C) Murine livers with *Mcl-1* deletion (*Mcl-1*$^{fl/fl}$, scAAV-LP1-Cre/scAAV-LP1-GFP) demonstrated relative elevation of long-chain fatty acylcarnitines compared to those

reconstituted with MCL-1 (*Mcl-1*$^{fl/fl}$, scAAV-LP1-Cre/scAAV-LP1-MCL-1). Error bars are mean ± S.D. for experiments performed in technical triplicate.

(D–E) MCL-1 western analysis of cellular lysates from tamoxifen-treated (d1–d3) *Mcl-1*$^{fl/fl}$CreER^{T2} + MCL-1^{OMM} and *Mcl-1*$^{fl/fl}$CreER^{T2} + MCL-1^{Matrix} MEFs at the indicated experimental time points (d1, d3, and d8; see experimental timeline, top) demonstrates the various levels of native and reconstituted MCL-1 protein isoforms (D), as also quantitated by densitometric analysis (E). Of note, reconstituted MCL-1^{Matrix} protein is composed of the mitochondrial localization sequence of ATP synthase fused to an N-terminally truncated MCL-1 (Perciavalle et al., 2012), accounting for the lower molecular weight compared to native MCL-1^{Matrix}.

(F) Fatty acylcarnitines were quantified from the indicated MEFs on experimental day 8. The sequential elevation of long-chain fatty acylcarnitines inversely correlated with the level of MCL-1^{Matrix} protein, rather than that of MCL-1^{OMM}, as reflected by the color sequence (black>gray>magenta>pink) (E). Error bars are mean ± S.D. for experiments performed in technical quadruplicate.

(G) Selective enrichment for BIM and PUMA by FLAG-MCL-1^{OMM}, and VLCAD by FLAG-MCL-1^{Matrix}, as evaluated by mass spectrometry of isoform-specific FLAG-MCL-1 immunoprecipitations from mouse liver mitochondria, which were isolated from *Mcl-1*$^{fl/fl}$ mice co-infected with scAAV-LP1-Cre and either scAAV-LP1-FLAG-MCL-1^{OMM} or scAAV-LP1-FLAG-MCL-1^{Matrix}. Each immunoprecipitation represents the pooled mitochondria from 3 independent mice, and the mass spectrometry analysis was performed in duplicate.

See also Figures S4–S5.

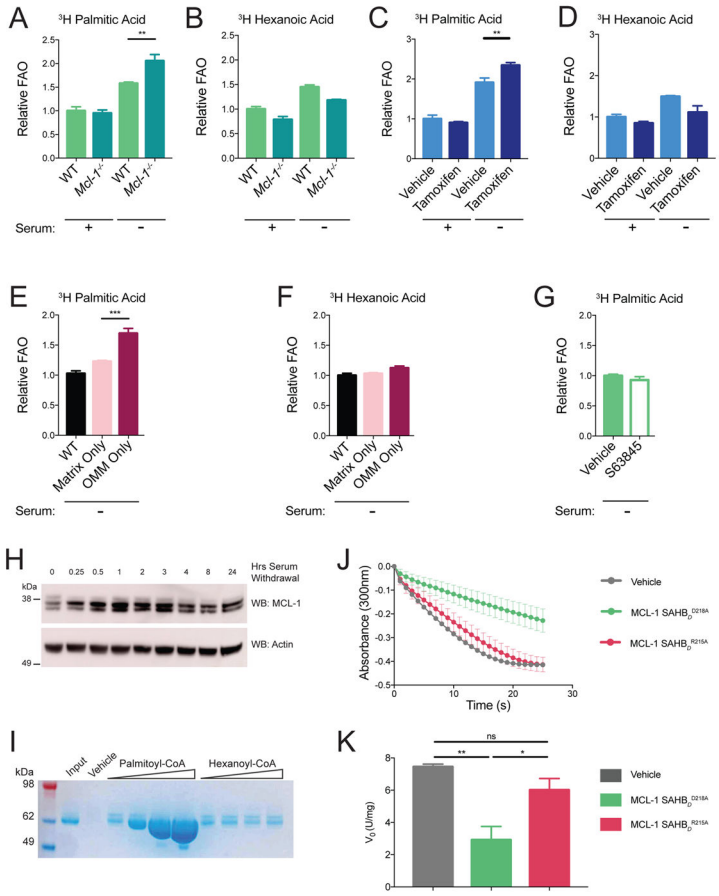

Figure 6. Dynamic Regulation of Long-Chain Fatty Acid Oxidation by MCL-1^{Matrix}

(A–B) Measurement of ^{3}H-palmitic acid (A) and ^{3}H-hexanoic acid (B) oxidation in wild-type and *Mcl-1*$^{-/-}$ MEFs in the presence and absence of serum. Error bars are mean ± S.D. for experiments performed in technical triplicate and repeated two (A) and four (B) times with similar results. **, $p < 0.01$.

(C–D) Measurement of ^{3}H-palmitic acid (C) and ^{3}H-hexanoic acid (D) oxidation in vehicle- or tamoxifen-treated *Mcl-1*$^{fl/fl}$CreER^{T2} MEFs, in the presence and absence of serum. Error bars are mean ± S.D. for experiments performed in technical triplicate and repeated two times with similar results. **, $p < 0.01$.

(E–F) Measurement of ^{3}H-palmitic acid (E) and ^{3}H-hexanoic acid (F) oxidation in tamoxifen-treated *Mcl-1*$^{+/+}$CreER^{T2} control cells and tamoxifen-treated MCL1^{OMM} or MCL-1^{Matrix}-reconstituted *Mcl-1*$^{fl/fl}$CreER^{T2} MEFs, under serum-starved conditions. Error bars are mean ± S.D. for experiments performed in technical triplicate and repeated two times with similar results. ***, $p < 0.001$.

(G) Measurement of ^{3}H-palmitic acid in vehicle- or S63845-treated wild-type MEFs under serum-starved conditions. Error bars are mean ± S.D. for experiments performed in technical triplicate and repeated two times with similar results.

(H) MCL-1 western analysis of lysates from wild-type MEFs subjected to the indicated duration of serum withdrawal. The experiment was performed twice with similar results.

(I) Streptavidin pull-down of biotinylated MCL-1 $SAHB_D$ upon titration of palmitoyl-CoA or hexanoyl-CoA, followed by recombinant VLCAD detection by electrophoresis and Coomassie staining.

(J) Effect of the indicated MCL-1 $SAHB_D$ constructs on the enzymatic activity of recombinant VLCAD. Error bars are mean ± S.E.M. for experiments performed in technical triplicate and repeated twice with similar results.

(K) Initial velocity of recombinant VLCAD calculated based on the slope of the enzyme kinetic curves (J). Error bars are mean ± S.E.M for experiments performed in technical triplicate and repeated twice with similar results. *, $p < 0.05$; **, $p < 0.01$.

See also Table S1.

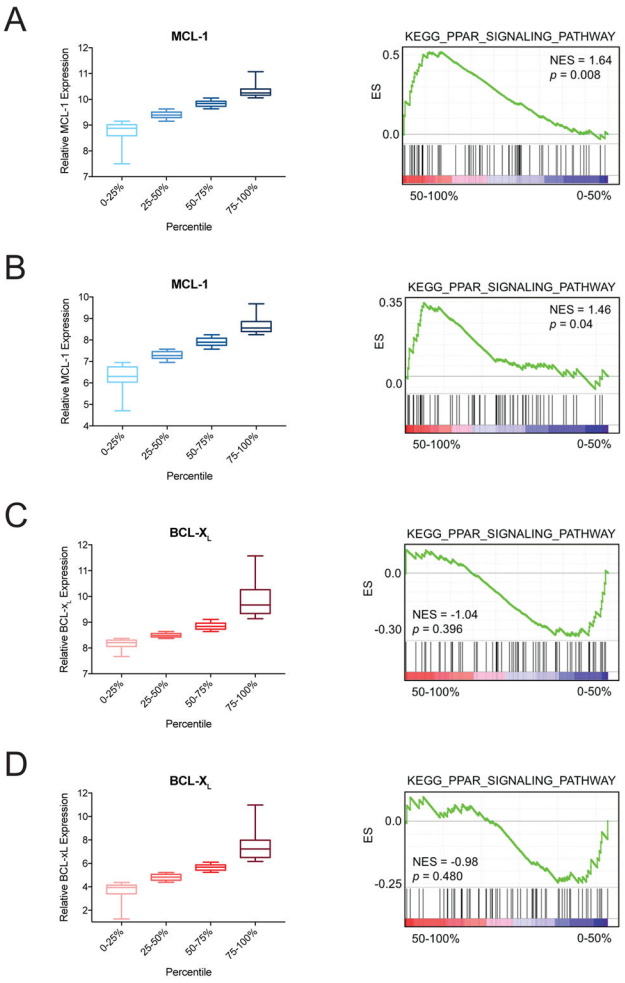

Figure 7. Correlation Between MCL-1 Expression Level and Fatty Acid Metabolism in AML

(A–D) Gene set enrichment analyses, performed on two distinct AML datasets, revealed a statistically significant correlation between MCL-1 expression level and a fatty acid β-oxidation signature (A–B). No such correlation was observed when the analysis was performed with an alternate anti-apoptotic BCL-2 family protein, BCL-X_L (C–D). Error bars represent minimum and maximum relative expression level values.